Department of Information Engineering and Computer Science

Master's Degree in
Computer Science

FINAL DISSERTATION

AUTOMATIC MEASUREMENT AND ANALYSIS OF PERIVASCULAR SPACES IN PARKINSONIAN SUBJECTS FROM BRAIN MRI IMAGES

Supervisor	Co-supervisor	Student
Paolo Giorgini	Selene Tomassini	Letizia Girardi

Academic year 2023/2024

Contents

1 Introduction **5**

2 Detection and segmentation of brain perivascular spaces: State-of-the-art **7**
  2.1 Perivascular spaces: Anatomy, function and clinical significance . . . 7
    2.1.1 Anatomy and physiology of perivascular spaces . . . 7
    2.1.2 Role of perivascular spaces in glymphatic system . . . 8
    2.1.3 Clinical significance of enlarged perivascular spaces . . . 8
    2.1.4 Imaging of perivascular spaces . . . 10
  2.2 Perivascular spaces enlargement in Parkinson's disease . . . 10
    2.2.1 Parkinson's pathology . . . 11
    2.2.2 Enlargement of perivascular spaces in Parkinson's disease . . . 11
    2.2.3 Clinical implications of perivascular spaces in Parkinsonian disorders . . . 12
  2.3 Perivascular spaces enlargement quantification . . . 12
    2.3.1 Search protocol . . . 12
    2.3.2 Search strategy . . . 14
    2.3.3 Search results . . . 15

3 Data **23**
  3.1 Study participants . . . 23
  3.2 Data acquisition . . . 23
  3.3 Ethical considerations . . . 24

4 Materials and methodology **25**
  4.1 Data preparation . . . 25
  4.2 Image-processing approach: Frangi filter-based . . . 29
    4.2.1 Detection of perivascular spaces . . . 29
    4.2.2 Segmentation of perivascular spaces . . . 35
  4.3 Deep-learning approach: 3D U-Net . . . 36
    4.3.1 Neural architecture . . . 36
    4.3.2 Segmentation of perivascular spaces . . . 41
  4.4 Volumetric rendering . . . 42

5 Experimental results **43**
  5.1 Segmentation task . . . 43
    5.1.1 Qualitative analysis: semi-automated approach vs automated approach . . . 43
    5.1.2 Quantitative analysis: semi-automated approach vs automated approach . . . 45
  5.2 Longitudinal study . . . 47

6 Conclusions **49**

Bibliography **51**

A List of acronyms **57**

B Ethical approval **59**

Summary

This dissertation describes in detail the activity performed during my Master thesis project at the University of Trento - Department of Information Engineering and Computer Science, which was supervised by Prof. Paolo Giorgini and Dr. Selene Tomassini. The study was conducted in collaboration with Prof. Quattrocchi, Director of the Radiology Department at Santa Maria del Carmine Hospital in Rovereto and received ethical approval from the Ethics Committee of the Fondazione Policlinico Universitario Campus Bio-Medical (approval number SC 2022.086).

This research originates from Prof. Quattrocchi's clinical observation that Parkinson's disease (PD) patients undergoing motor exercise therapy exhibited a reduction in perivascular spaces (PVS) volume after one month of treatment.

PVS are small fluid-filled cavities surrounding the blood vessels in the brain that play a fundamental role in brain homeostasis by facilitating the clearance of metabolic waste products. They support the brain's self-cleaning mechanism, known as the glymphatic system. Under normal conditions, PVS are barely visible on neuroimaging scans, typically measuring less than 2-3 mm in diameter. However, they can multiply and change in size as a result of ageing, vascular changes or neurodegeneration. Enlarged PVS has been increasingly associated with various neurodegenerative disorders, including PD.

In the context of PD, PVS has been defined as key biomarker for the disease progressions, indicating that PVS alterations in number and dimensions could reflect disease severity and help in predicting which patients are more likely to experience faster functional deterioration. Additionally, strong correlations between PVS and non-motor symptoms of PD, including cognitive decline, mood disorders and sleep disturbance. Given their involvement in these key aspects of the disease, PVS have the potential to serve as imaging biomarker, helping in both early diagnosis and monitoring of PD degeneration.

Under the clinical observation and request of the Prof. Quattrocchi, this research focuses on developing a decision-support system for detecting and segmenting PVS in brain MRI scans in order to analyze their dynamicity over time, processing a dedicated dataset of PD patients. By leveraging advanced image processing and deep learning techniques, this study aims to provide more accurate, efficientand reproducible quantification of PVS, improving their clinical utility in assessing disease progression and response to therapeutic interventions.

From a technical viewpoint, the contribution lies in the implementation of a 3D U-Net to address the specific challenges related to the segmentation of PVS, taking into account their dimensional variation and the difficulty of distinguishing them from other brain microstructures. A semi-automatic yet clinically-validated approach was adopted for the construction of the ground truths to overcome the lack of annotations for a reliable segmentation outcome. Specifically, the PVS maps were generated by applying a modular pipeline converging in a Frangi filter, a technique consolidated in the literature for the extraction of tubular structures from medical images. An in-depth statistical analysis was then performed to verify if and in which cases the volume of delineated PVS were correlated with clinically-relevant variables. This analysis revealed clinical correlations in three cases. In fact, PVS volume positively correlated with UPDRS III scores (Unified Parkinson's Disease Rating Scale, Part III - motor examination), indicating that higher PVS volume is associated with more severe motor symptoms; whereas, a negative correlation was found between PVS volume and sleep duration (both median and average), suggesting that reduced sleep may contribute to PVS enlargement.

From a clinical viewpoint, processed MRI scans belonging to a subset of PD patients representative of all participants to the trial underwent to a longitudinal analysis to asses changes in dynamicity of PVS volume before (i.e. at time point 0, T0) and after (i.e. after one month, T1) the motor therapy. This further analysis showed that 100% of subjects experienced a reduction in the PVS volume, supporting the initial clinical

hypothesis of Prof. Quattrocchi, thus reinforcing the relevance of PVS changes in PD monitoring.

To summarize, the proposed framework is capable of recognizing a PVS structure from other brain microstructures in MRI data, counting the number of similar structures and computing the total volume composing the whole glymphatic system. The study also demonstrates the clinical utility of automated PVS quantification as a potential imaging biomarker for PD. Specifically, the computation of PVS total volume within the white matter allowed to observe strong associations beetween PVS dimensions, motor symptoms and sleep disturbances, providing new insights into PD pathophysiology and suggesting a novel approach for PD analysis and therapeutic treatments.

Despite our proposed framework has been significantly evaluated both quantitatively and qualitatively in terms of detecting and localizing structures of interest, further improvements are needed. In particular, improving data resolution, expanding the dataset through strategies other than training data augmentation, or including a larger number of participants could help to further improve the accuracy and reliability of the model, making it even more robust and applicable in real clinical settings and allowing for even more precise clinical analyses.

Chapter 1

Introduction

Perivascular spaces (PVS), also known as Virchow-Robin spaces, are small fluid-filled compartments surrounding blood vessels in the brain (Wardlaw et al., 2020), widely known for their significant role in maintaining fluid balance, supporting brain homeostasis and ensuring proper neurological function. In recent years, increasing interest has been directed towards their study, particularly due to emerging evidence linking PVS enlargement to various neurodegenerative diseases and cognitive decline. Understanding the anatomy, function and clinical relevance of PVS is, therefore, essential to investigate their role in conditions such as Alzheimer's disease, stroke and small vessel disease. Under normal conditions, PVS are quite small, typically measuring less than 2-3 mm in diameter. However, they can multiply or change in size as a result of ageing, vascular changes or neurodegeneration. Thanks to current developments in neuroradiological imaging technologies, despite their small size, they are quite visible and can be studied. Specifically, PVS visible on MRI are referred to as enlarged PVS.

Emerging research suggests that increased PVS can have significant clinical consequences, including dementia. This phenomenon is observed in several neurodegenerative diseases, including Parkinson's disease (PD). PD mainly affects movement, but is also associated with a variety of motor and non-motor symptoms. Patients with PD often show tremors, rigidity, bradykinesia and gait abnormalities such as freezing, which impair their ability to perform daily activities and negatively impact their quality of life. A study by Wan et al. (2019) showed a connection between PVS and tremor severity in PD patients. This result allows us to hypothesize that, by recognizing associations between motor symptoms and PVS, we can better predict the presence and intensity of motor symptoms in patients affected with PD, facilitating and managing these pathological aspects of the disease. In addition to motor symptoms, the disease is often paired with cognitive symptoms and psychiatric conditions, such as depression and anxiety, which tend to worsen as the disorder progresses (Bhat et al., 2018). Furthermore, the brain's glymphatic system, which is closely dependent on PVS and responsible for the elimination of metabolic wastes and toxins, is often impaired in PD. Specifically, the accumulation of alpha-synuclein proteins, together with other neuro-toxic substances that form Lewy bodies, impairs lymphatic function and can accelerate the neurodegeneration process. Therefore, PVS not only serve as a marker for disease progression, but may also be a contributing factor to neurodegeneration Fang et al. (2020).

The visualization of PVS with neuroimaging, mainly magnetic resonance imaging (MRI), provides valuable information on brain conditions and is currently the gold standard for their in vivo assessment in humans (Pham et al., 2022). PVS examination is spreading as an emerging biomarker to better understand PD pathology. In recent years, advances in biomarker discovery, genetic studies and neuroimaging have contributed to a deeper understanding of PD, although its clinical diagnosis remains difficult due to the variability of symptoms.

Building on these findings, the clinical objective of this study is to prove whether the PVS in PD patients decreases in both number and volume following a one-month treatment protocol that includes a combination of memory and motor exercises performed daily for 30 minutes. Beyond the clinical objective, this thesis focuses on developing two methods, one semi-automatic and the other fully-automatic, for segmenting PVS in T1-weigthed MRI scans, using a dedicated dataset of PD patients. More in detail, the main contribution from a technical viewpoint lies in the implementation of a 3D U-Net to address the specific challenges related to the segmentation of PVS, taking into account their dimensional variation and the difficulty of distinguishing them from other brain structures. However, training deep learning models requires reliable ground truths, i.e. valid segmentation of the structures of interest. This process, if manual, is extremely time-consuming, laborious and impractical, especially considering that PVS are very small and numerous structures. Thus, a semi-automatic approach was adopted for the construction of the ground truths to overcome this limitation and ensure greater reliability of the results. Specifically, the PVS maps were generated by applying a modular pipeline converging in a Frangi filter, a technique consolidated in the literature for the extraction of tubular structures from medical images. Subsequently, an expert neuroradiologist performed a manual correction and approval, ensuring a more accurate and clinically-valid annotation. From a clinical viewpoint, the correlations between PVS enlargement and PD progression were analyzed, with the aim of evaluating how these brain structures change over time. In particular, the effect of the above mentioned treatment was studied, examining its clinical implications and its impact on the morphology of PVS during the course of the disease.

The study is performed in collaboration with Prof. Quattrocchi, Director of the Radiology Department of Santa Maria del Carmine Hospital in Rovereto and has received approval from the Ethics Committee of the Fondazione Policlinico Universitario Campus Bio-Medical (n. SC 2022.086). Written informed consent was obtained from all participants prior to their involvement, ensuring their understanding and voluntary participation.

The rest of the dissertation is organized as follows. Chapter 2 provides an overview of the state-of-the-art in PVS detection and segmentation, presenting the most recent methodologies and clinical studies in the field. Chapter 3 describes in details the custom-made dataset, including the MRI acquisition techniques and the relevant information about the study participants. Chapter 4 describes how detection and segmentation has been achieved by the two methods. Chapter 5 reports the experimental results obtained, whereas Chapter 6 concludes the dissertation by summarizing key finding and discussing future research directions.

Chapter 2

Detection and segmentation of brain perivascular spaces: State-of-the-art

2.1 Perivascular spaces: Anatomy, function and clinical significance

PVS, also known as Virchow-Robin spaces, are small, fluid-filled compartments that surround blood vessels in the brain (Wardlaw et al., 2020), acting as vital channels for fluid exchange between the cerebrospinal fluid (CSF) and the surrounding interstitial space. Although initially considered incidental imaging findings, PVS are now recognized for their significant role in maintaining fluid balance, supporting cerebral homeostasis and ensuring proper neurological function.

In recent years, growing interest has been directed to the study of PVS, particularly due to emerging evidence that links the enlargement of PVS to various neurodegenerative diseases and cognitive decline. Understanding the anatomy, function and clinical relevance of PVS is, therefore, essential for investigating their role in conditions such as Alzheimer's disease, stroke and small vessel disease.

2.1.1 Anatomy and physiology of perivascular spaces

Structurally, PVS are tubular, fluid-filled channels that follow the path of blood vessels as they penetrate deep into the brain tissue (Wardlaw et al., 2013). They are especially concentrated in regions with a high density of small blood vessels, such as the basal ganglia and the centrum semiovale. They typically surround arterioles and capillaries and, more rarely, veins, as these vessels penetrate the brain tissue 2.1. This distribution allows the exchange of fluids between the brain's interstitial spaces and the CSF, helping to regulate fluid movement and support the brain's waste clearance systems Gouveia-Freitas and Bastos-Leite (2021).

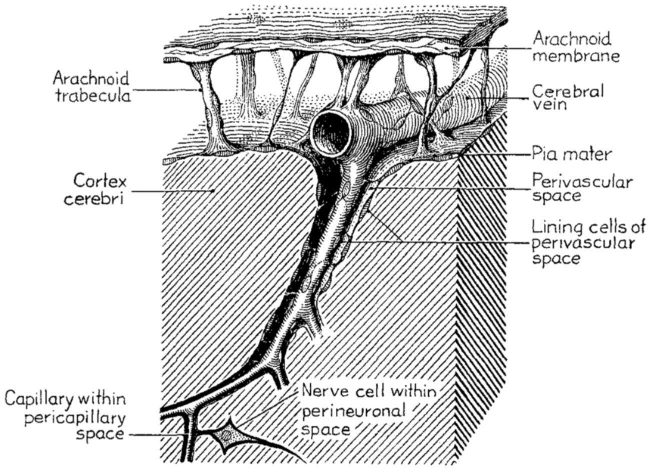

Figure 2.1: Schematic representation of PVS according to Weed et al. (1923).

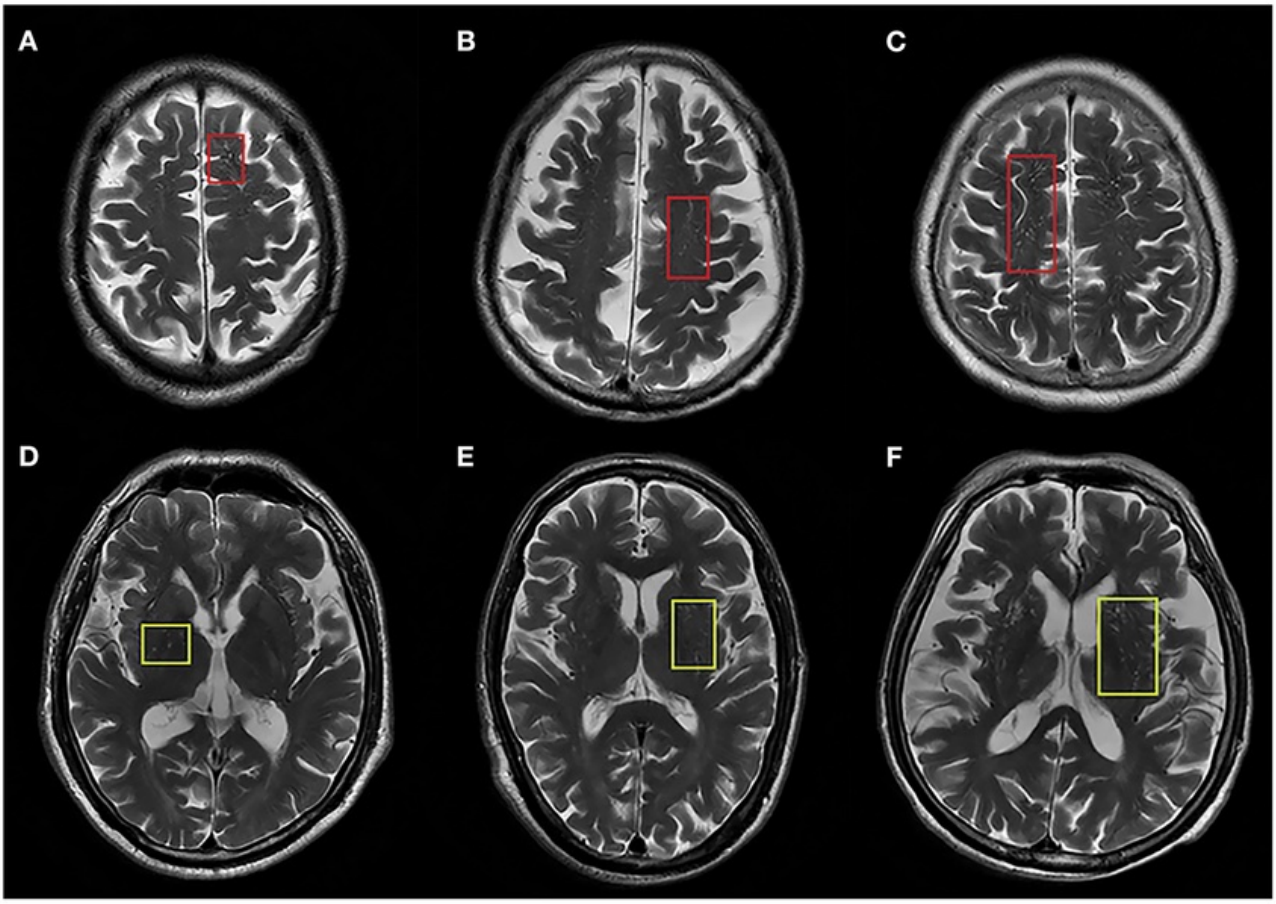

Figure 2.2: Representative axial T2-weighted MRI images of ePVS in centrum semiovale (PVS-CSO) and basal ganglia (PVS-BG). (A–C) Indicate PVS-CSO with red squares corresponding to degree of severity. (D–F) Indicate PVS-BG with yellow squares corresponding to degree of severity (Shen et al., 2021).

2.1.2 Role of perivascular spaces in glymphatic system

PVS are involved in the drainage of waste products from the brain, a process also known as the "glymphatic" system (Gouveia-Freitas and Bastos-Leite, 2021). The glymphatic system is a waste disposal system, similar to the lymphatic system in the rest of the body, based on a network of perivascular channels, formed by astroglial cells, cells specialized in removing soluble proteins and metabolites from the central nervous system (Jessen et al., 2015).

The brain consists of four fluid compartments: CSF, interstitial fluid (ISF), intracellular fluid and the blood vasculature (Figure 2.3a). In glymphatic system, the focus is on the interaction and regular exchange between CSF and ISF. Briefly, CSF enters the brain through the PVS surrounding cerebral arteries. As it moves deeper into the brain, it mixes with ISF and parenchymal solutes. This fluid, now carrying the brain's waste, is drained out of the brain through PVS around veins into the body's lymphatic system, where it can be definitely removed. Clearance of soluble proteins, waste products and excess extracellular fluid is facilitated by astrocytic aquaporin 4 (AQP4) water channels. PVS are surrounded by astrocytes which are rich in AQP4 channels 2.3b. These channels makes the movement of fluids between the PVS and the brain's extracellular space easier, helping to remove metabolic waste from the brain.

2.1.3 Clinical significance of enlarged perivascular spaces

Under normal conditions, PVS are very small, typically measuring less than 2–3 mm in diameter. However, factors such as aging, vascular changes, or neurodegenerative diseases can cause them to enlarge and become more numerous. When these spaces are visible in vivo on MRI (Figure 2.4a), they are referred to as ePVS (Wardlaw et al., 2020). In some cases, PVS can enlarge dramatically, forming what is known as tumefactive PVS 2.4b, which are over 15 mm in diameter and can mimic cyst-like lesions on imaging. Such extreme

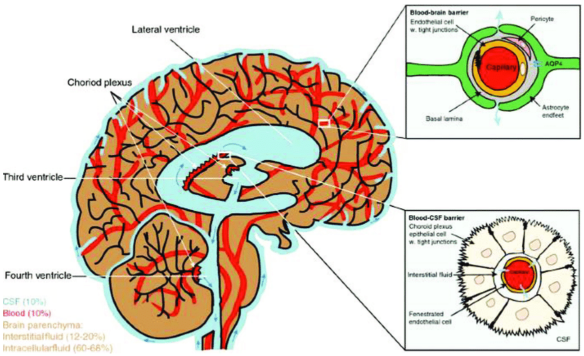

(a) Schematic representation of the brain's fluid compartments and barriers (Jessen et al., 2015).

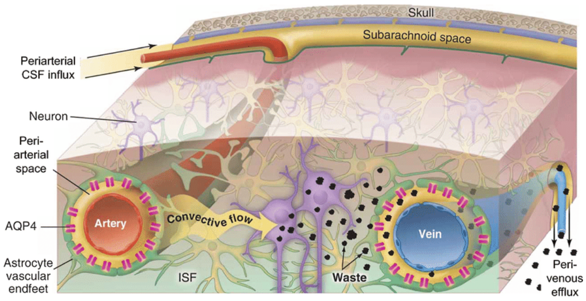

(b) Perivascular glymphatic transport in the brain. Schematic depicting the proposed mechanism underlying molecular transport in brain tissue, the glymphatic system (Ray et al., 2021).

enlargement is rare but highlights the potential for PVS to become significantly dangerous in pathological states.

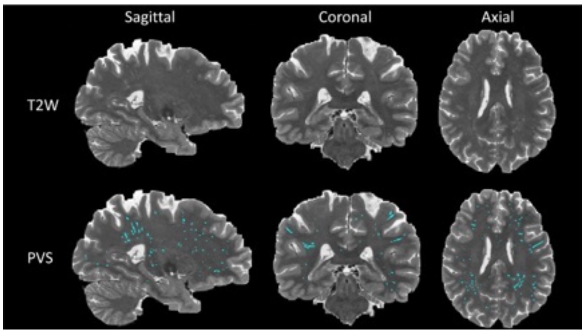

(a) PVS map segmented by an AI-based algorithm. First row is the T2-weighted modality of one subject with sagittal, coronal and axial view. Second row is the PVS map (cyan) overlaid on T2-weighted modality from the same subject.

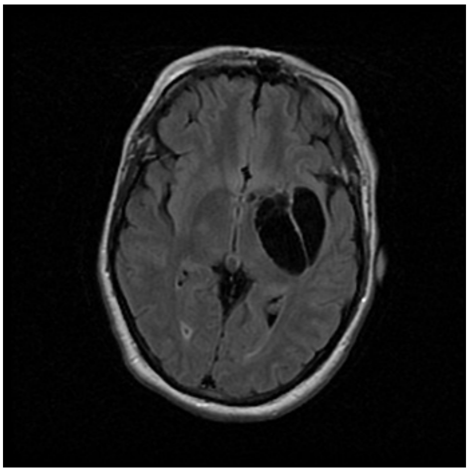

(b) Tumefactive PVS. Axial FLAIR. Parkinsonian woman, 50 years old.

Figure 2.4: Scans with PVS at different level of dimension.

Historically, PVS were considered benign and seen as an epiphenomenon of neurodegeneration. However, emerging research suggests that PVS may have clinical consequences. Multiple studies now support the theory that PVS are associated with dementia, yet an important ongoing debate is whether PVS contribute to cognitive impairment or are merely a by-product of other disease processes.

Several studies in mice have demonstrated impaired glymphatic clearance, which may explain the higher prevalence of these diseases in older adults (Kress et al., 2014). Proteins such as tau and amyloid-beta, both associated with Alzheimer's, are cleared from the brain through the glymphatic system. In Alzheimer's disease, the accumulation of these proteins leads to larger PVS, likely due to the brain's inability to effectively clear these toxic substances. Research shows that Alzheimer's patients have significantly more ePVS compared to healthy individuals, suggesting a link between poor glymphatic drainage and the buildup of proteins central to neurodegenerative diseases (Iliff et al., 2014). However, ePVS are also emerging as potential biomarkers for poor glymphatic function in conditions like multiple sclerosis and PD (Moses et al., 2023). In sclerotic patients, PVS have been observed at higher levels than in healthy controls, pointing to a connection between inflammation and PVS expansion. PVS size has also been shown to increase in response to active disease episodes. Similarly, in PD an increased volume and number of PVS in the basal ganglia have been associated with disease severity, suggesting PVS could serve as a marker for tracking PD progression (Shen et al., 2021).

2.1.4 Imaging of perivascular spaces

The visualization of ePVS in neuroimaging provides valuable insights into brain conditions. MRI is the current standard for in vivo assessment of PVS in humans (Pham et al., 2022). These spaces are typically observed using T1-weighted, T2-weighted and FLAIR sequences.

On MRI, the appearance of PVS varies depending on both the imaging sequence and the plane of orientation. On T1-weighted images, where fat and soft tissues appear bright, PVS show up as dark, hypointense areas. In contrast, on T2-weighted images, which emphasize fluid, PVS appear bright and hyperintense, making them easier to identify (Kwee and Kwee, 2007). Their shape on MRI is influenced by their alignment with the imaging plane. They can appear as either linear or round structures, depending on their orientation relative to the imaging plane. They are visualized as elongated structures when aligned parallel, sagittal view, to the imaging plane and as dots when viewed perpendicularly, axial view, (Choi et al., 2020). Moreover, the visibility of PVS on MRI is significantly influenced by the magnetic field strength and the resolution of the image. While 1.5 Tesla MRI may struggle to visualize PVS when they are not enlarged, higher field strengths of 3 Tesla or higher may provide better resolution. This allows for clearer visualization of PVS morphology, even in healthy individuals like adolescents and young adults, where visible PVS do not necessarily indicate pathology (Barisano et al., 2021).

Therefore, quantifying the size, number and distribution of PVS is crucial for understanding and potentially preventing different neurological conditions such as AD, PD and small vessel disease. Modern machine learning techniques, including convolutional neural networks, are being trained to automatically detect and quantify PVS, allowing for deeply statistical analysis, i.e. correlation between the number of perivascular spaces and hours of sleep, age or other factors.

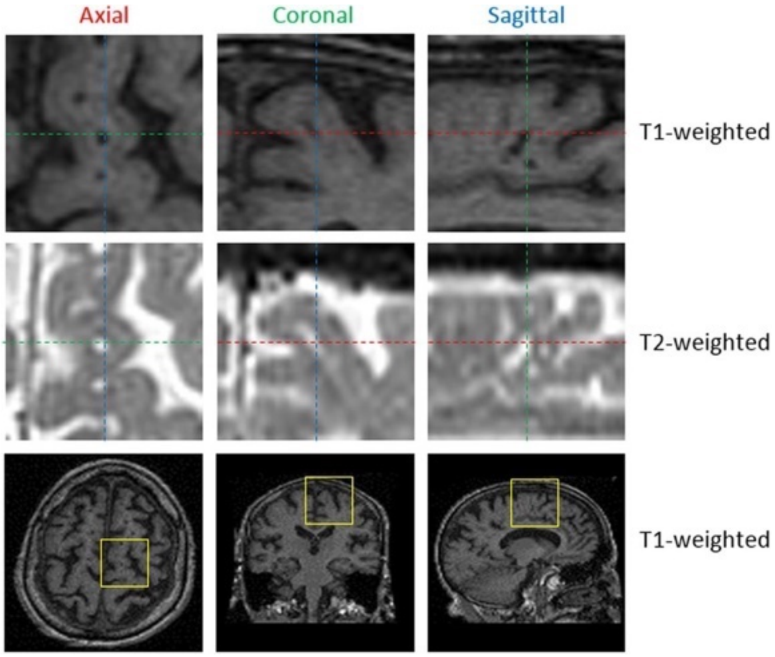

Figure 2.5: Magnified view of PVS in an axial, coronal and sagittal slice in T1-weighted and T2-weighted MRI images. The position of these zooms in corresponding T1-weighted brain scans is highlighted with yellow squares (bottom row) (Ballerini et al., 2018).

2.2 Perivascular spaces enlargement in Parkinson's disease

PD is a complex and progressive neurodegenerative disorder primarily affecting movement, along with a range of other motor and non-motor symptoms. It typically manifests with tremors, rigidity, bradykinesia and gait abnormalities like freezing, making daily activities increasingly difficult and impacting patients' quality of life. Additionally, PD frequently presents with cognitive symptoms and psychiatric conditions such as depression and anxiety, which can worsen as the disease advances (Bhat et al., 2018). The disease is characterized by the degeneration of dopamine-producing neurons in the substantia nigra—a crucial area for movement regulation—and is also marked by the abnormal buildup of alpha-synuclein proteins (Lewy bodies) in the brain (Kobylecki, 2020).

2.2.1 Parkinson's pathology

Different are the underlying biological and structural changes in the brain that characterize PD. Mainly, when dealing with PD, we have to consider:

- *Dopaminergic neuron degeneration*: The primary feature of Parkinson's pathology is the progressive loss of dopamine-producing neurons in the substantia nigra, a part of the brain involved in movement control. This loss leads to decreased dopamine levels, disrupting smooth and coordinated movements and resulting in the characteristic motor symptoms of PD, such as tremors, rigidity and bradykinesia.

- *Lewy Bodies and alpha-synuclein aggregation*: PD is also marked by the accumulation of Lewy bodies within neurons. These abnormal protein clumps, primarily composed of alpha-synuclein, interfere with cellular functions and are believed to contribute to cell death. The exact role of Lewy bodies in disease progression is still under study, but their presence is a hallmark of PD pathology.

- *Neuroinflammation*: Increasing evidence shows that neuroinflammation—marked by the activation of microglia[1] contributes to the progression of PD. Neuroinflammation may be a response to the accumulation of misfolded alpha-synuclein, which triggers an immune response that, while aimed at clearing the proteins, may inadvertently damage healthy neurons.

- *Vascular dysfunction*: Recent studies suggest that vascular changes, including impaired blood flow and small vessel damage, also play a role in PD pathology. These vascular issues can disrupt the brain's ability to clear waste products and provide essential nutrients, potentially exacerbating neurodegeneration.

These pathological changes contribute to the progression of PD thus understanding PD pathology is crucial for developing targeted treatments.

In recent years, advancements in biomarker discovery, genetic studies and neuroimaging have contributed to a deeper understanding of PD. However, due to the variability of its symptoms, clinical diagnosis still remains really challenging. Complex machine or deep learning techniques have been explored to enhance and improve diagnostic accuracy and efficiency, predict disease progression and identify biomarkers (Nilashi et al., 2023).

2.2.2 Enlargement of perivascular spaces in Parkinson's disease

The cerebral glymphatic system is a specialized elimination pathway for metabolic wastes and toxins. In PD, this system is often compromised by the accumulation of alpha-synuclein proteins and other neurotoxic substances that form clusters known as Lewy bodies with neurons, impairing lymphatic function and potentially accelerating neurodegeneration. Thus, PVS may serve both as a marker of disease progression and as a potential contributing factor to its progression.

Ma et al. (2021) thoroughly examined the role of the glymphatic system in PD using diffusion tensor imaging analysis along PVS (DTI-ALPS) and calculating diffusivity along PVS (ALPS). The ALPS index is a quantitative measure of water diffusivity in specific brain regions and is calculated to provide insight into lymphatic clearence. Low values suggest impaired fluid clearance. Results showed that patients with PD have a significantly lower ALPS index than controls, indicating impaired glymphatic function, potentially related to protein accumulation and neuroinflammation in PD. Similarly, Meng et al. (2024) analyzed PVS by evaluating DTI-ALPS indices in the bilateral hemispheres and counting the number of PVS in the bilateral CSO, BG and midbrain. The results showed that patients with PD have significantly lower DTI-ALPS indices and higher numbers of PVS, particularly in patients in the mid-late phase and within the BG. In

---

[1] microglia: immune cells in the brain

addition, both DTI-ALPS indices and the number of PVS were found to correlate with age and PD progression, suggesting their potential as noninvasive measures for assessing glymphatic dysfunction in PD. More recently, (Yao et al., 2024) extended the analysis of glymphatic function in PD using a hybrid positron emission tomography (PET)-MRI approach combined with diffusion tensor imaging along PVS (DTI-ALPS) and PVS volume. This study included 25 patients with PD and 30 healthy controls, analyzing glymphatic dysfunction in relation to clinical severity and the extent of dopaminergic neuron loss in PD. Their results are in line with those of previous studies, which have shown that PD patients have significantly lower DTI-ALPS indices and higher PVS volume than healthy controls (Yao et al., 2024), (Donahue et al., 2021). Notably, the DTI-ALPS index was negatively correlated with the severity of motor symptoms. The relationship between reduced glymphatic function and increased markers of neurodegeneration, as measured by both DTI-ALPS and PET, highlights the usefulness of multimodal imaging in understanding and following the progression of PD. Together with the results of (Meng et al., 2024), these findings reinforce the idea that glymphatic dysfunction may be a valuable noninvasive biomarker for disease progression in PD.

2.2.3 Clinical implications of perivascular spaces in Parkinsonian disorders

Research increasingly highlights the importance of PVS in PD, particularly in brain areas essential for motor control such as the BG and midbrain. Wan et al. (2019) showed a connection between PVS and tremor severity in PD patients. This result allows us to hypothesize that by recognizing associations between motor symptoms and PVS, we can better predict the presence and intensity of motor symptoms in PD patients, facilitating and managing these pathological aspects of the disease. Furthermore, studies such as Fang et al. (2020) have related lower levels of BG-PVS biomarkers with rapid progression on the Hoehn & Yahr scale, particularly in patients who were at stage 1 at baseline. These findings suggest that BG-PVS could serve as a valuable predictor of disease progression in Parkinson's disease. This suggests that BG-PVS might not only serve as a marker of disease progression, but also provide a way to identify patients who might experience more rapid functional decline.

Although the relationship between PVS and motor symptoms in PD has mainly been explored, they have a significant effect in a broader context, namely the impact on cognitive function and other non-motor aspects. Cognitive impairment is a common and debilitating component of PD, especially in the advanced stages. PVS have been found to be closely linked to cognitive decline in PD patients. They can contribute to cognitive decline, mood disorders and autonomic function, such as sleep disturbances. Studies conducted by Gui et al. (2024) and Luo et al. (2024) have related increased PVS and lower values of DTI-ALPS indices to cognitive decline and sleep disorders. In particular, PD patients with non-motor symptoms, regardless of their type, showed *higher levels of PVS, with even higher PVS counts in subjects with cognitive impairment*, compared with control subjects. These results highlight how monitoring changes in glymphatic function, reflected in BG-PVS severity, can help detect and predict cognitive decline in PD (Luo et al., 2024).

2.3 Perivascular spaces enlargement quantification

In this chapter, we outline the methodology used to conduct a systematic literature review on PVS enlargement, specifying the research questions that guided the selection of articles, the criteria used to identify relevant studies and the approach for data extraction. This methodology is designed to be comprehensive and unbiased.

2.3.1 Search protocol

In Figure 2.6, the outline of our search protocol aimed at identifying valid methods to quantify PVS.

Search questions

The search questions formed the framework for the entire study, helping narrowing the literature search and selecting the most relevant articles. To guide the search, we formulated several key questions to ensure a comprehensive and systematic approach:

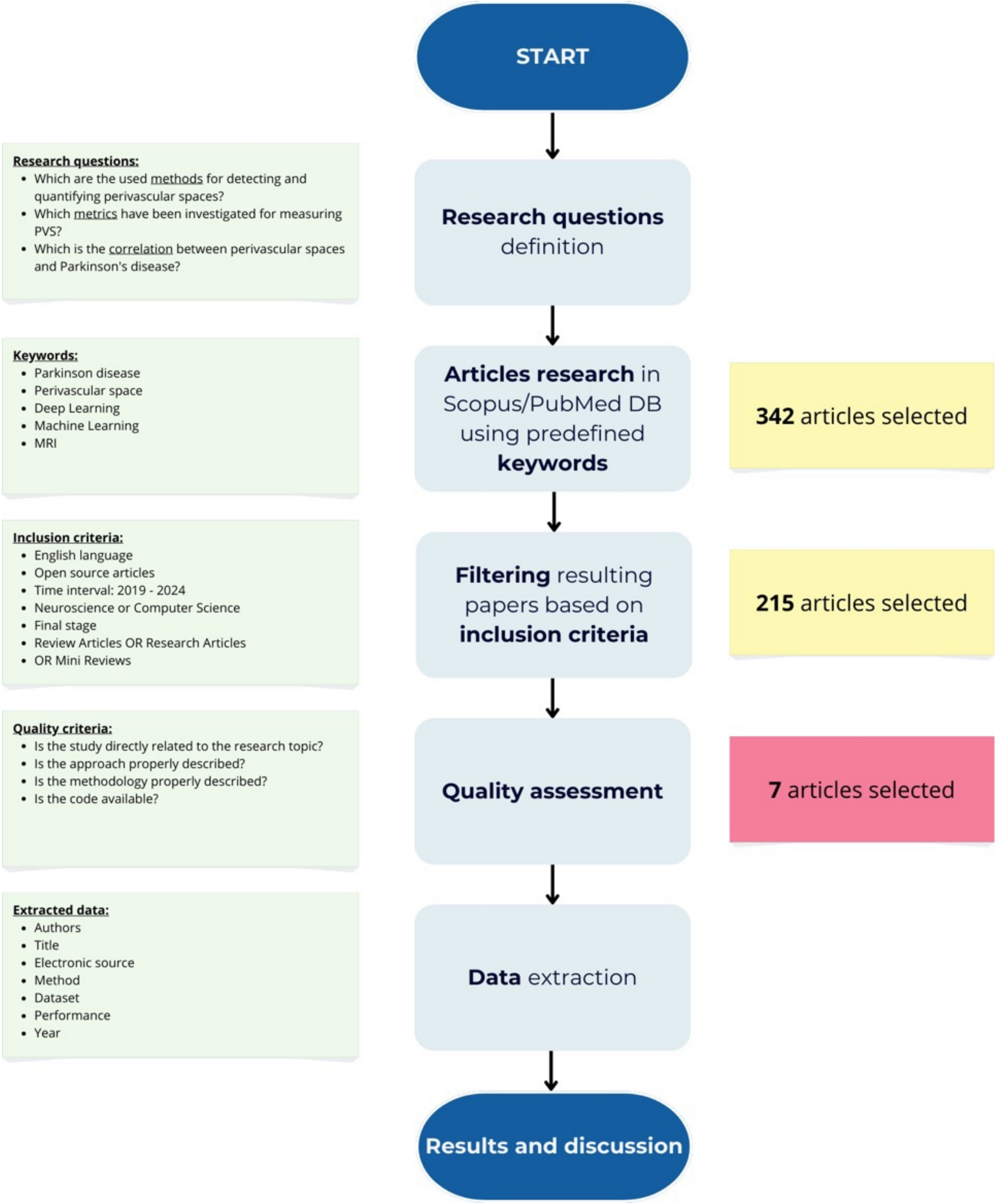

Research questions:
- Which are the used methods for detecting and quantifying perivascular spaces?
- Which metrics have been investigated for measuring PVS?
- Which is the correlation between perivascular spaces and Parkinson's disease?

Keywords:
- Parkinson disease
- Perivascular space
- Deep Learning
- Machine Learning
- MRI

Inclusion criteria:
- English language
- Open source articles
- Time interval: 2019 - 2024
- Neuroscience or Computer Science
- Final stage
- Review Articles OR Research Articles
- OR Mini Reviews

Quality criteria:
- Is the study directly related to the research topic?
- Is the approach properly described?
- Is the methodology properly described?
- Is the code available?

Extracted data:
- Authors
- Title
- Electronic source
- Method
- Dataset
- Performance
- Year

Figure 2.6: Schematic representation of the search protocol for identifying valid methods to quantify PVS in the brain.

- **What are the current state-of-the-art methods for quantifying PVS in brain MRI scans?** - This question seeks to identify and evaluate the various techniques used in imaging and analysis to detect and measure PVS.
- **Which metrics are used to validate the performance of PVS quantification methods?** - This question seeks to explore the different metrics (e.g. volume, number, size) employed in previous studies to assess the method.
- **How do different approaches compare in terms of accuracy and reliability for quantifying PVS?** - This question focuses on comparing the effectiveness and precision of various PVS quantification technique.
- **What are the key challenges and limitations in the current methods for quantifying PVS in brain MRI scans?** - This question aims to uncover the common challenges faced in the existing methods.

2.3.2 Search strategy

A comprehensive search strategy was employed to systematically collect relevant literature using two major databases: Scopus and PubMed. These databases were selected for their broad coverage of biomedical, engineering and technical literature, which is essential for an in-depth exploration of the clinical and methodological aspects of PVS and PD research.

Search keywords The analysis was conducted using a set of carefully chosen keywords used both individually and in combination to maximize the search for relevant studies. Boolean operators (AND, OR) were used to refine and narrow the search results.

Inclusion criteria To ensure relevance, the search was limited to articles published between 2019 and 2024. This time frame was chosen to capture the most recent advancements in the field. In addition, inclusion criteria were designed to filter the search results, ensuring that only studies relevant to the research questions and objectives were included in the review. Specifically, the inclusion criteria were as follows:

- *Language:* Only articles published in English were included so that all studies could be fully understood and accurately interpreted.
- *Accessibility:* The review focused on openly-accessible articles to ensure that the data could be freely accessed and verified by others, promoting transparency and reproducibility.
- *Time interval:* The search was limited to studies published between 2019 and 2024, in line with the need to examine contemporary research reflecting the latest developments in the field.

Quality assessment The quality assessment was a critical step in ensuring that only methodologically sound and relevant studies were included in the final analysis. This process involved a detailed review of each article against the following criteria:

- *Relevance to research topic:* Each study was assessed to ensure that it directly addressed the research questions related to the topic. Studies that were only tangentially related or that focused on unrelated aspects were excluded.
- *Description of methodology:* The clarity and comprehensiveness of the methodological description in each study were evaluated. Studies that lacked sufficient detail in their methodology or failed to describe their procedures clearly were excluded.
- *Approach proposed:* The studies were reviewed to determine whether the methods and approaches used were appropriate for the research questions being addressed. Studies that used outdated or inappropriate methods were excluded.
- *Availability of code/data:* For studies involving computational methods, the availability of code or datasets was considered. Studies that did not provide access to these resources were critically evaluated for their transparency.

Data extraction Data extraction involved systematically collecting information from each of the selected studies to facilitate a comprehensive analysis. The extracted data included:

- *Authors:* The names of the researchers who conducted the study.
- *Title:* The full title of the study, offering insight into the focus and scope of the research.
- *Proposed method:* A detailed description of the methods used, which is critical for comparing and evaluating the effectiveness of different approaches.
- *Dataset:* Information on the datasets used in the study, including size, type and source, which is essential for assessing the study's applicability.
- *Performance:* The reported performance metrics (e.g. accuracy, sensitivity, specificity) of the methods used, providing a basis for comparing the effectiveness of different techniques.
- *Year:* The year of publication, contextualizing the study within the timeline of research developments.

2.3.3 Search results

By querying online databases using the search strategies described in Table 2.1, we retrieved a total of 342 articles. After applying the inclusion criteria as in 2.3.2, the number of valid articles was reduced to 215 articles. In the final stage, after quality assessment as in 2.3.2, the number of relevant studies was further reduced to 8 articles.

Query	**# Results**	**# Filtering results**	**# Selected papers**
Quantifying PVS	65	21	4
Quantifying PVS or Virchow-Robin	136	79	7
Learning algorithms for PVS	141	115	12
Total	**342**	**215**	**7**[2]

Table 2.1: Summary of the literature search process, including queries used, the number of initial results, the number of filtered results and the selected papers.

Table 2.2 presents an overview of data extracted from multiple studies, highlighting key details such as the authors' names, publication year, image sequence and specific brain regions examined. Information on the datasets used and the evaluation metrics employed to assess the methodologies of each study was included.

---

[2] The total selected papers, excluding any instances of duplication in the selection process and review.

Ref.	Proposed method	Imaging technique	Brain area	Dataset	Note
(Huang et al., 2024)	mcPVS-Net	3D T1 and T2-weighted MRI	BG and WM	ADNI, including 40 training and 15 test subjects	DSC = 0.80, Precision = 0.81, Recall = 0.79
(Cai et al., 2024)	multi-scale supervised dense nested attention network	T2-weighted 3T MRI	BG and CSO	20 patients with PD (42–79 years)	DSC = 0.70; strong correlation with expert scoring
(Rashid et al., 2023)	U-Net	SWI, FLAIR, T1 and T2-weighted MRI	Whole brain	21 participants from the MESA cohort	T2-weighted MRI was the most informative for PVS detection, with minor improvements from adding SWI, FLAIR and T1-wwighted. Sensitivity = 0.82, Precision = 0.83, DSC = 0.61
(Spijkerman et al., 2022)	binary kNN classifier	T2-weighted TSE scans (higher resolution)	CSO	50 subjects with manual annotations	DCS = 0.61, excludes small PVS (<2mm)
(Boutinaud et al., 2021)	autoencoder and U-Net	T1-weighted MRI	DWM and BG	1832 healthy young adults	Good agreement with visual ratings; NA
(Dubost et al., 2019b)	regression-based 3D CNN	T2-weighted MRI	Midbrain, hippocampi, BG and CSO	2115 subjects from a population-based study	ICC: 0.75-0.88

Table 2.2: Existing automated methods for quantifying PVS.

Perivascular spaces quantification pipeline

Based on the achieved results, the pipeline for the quantification of PVS (Figure 2.7) may involve:

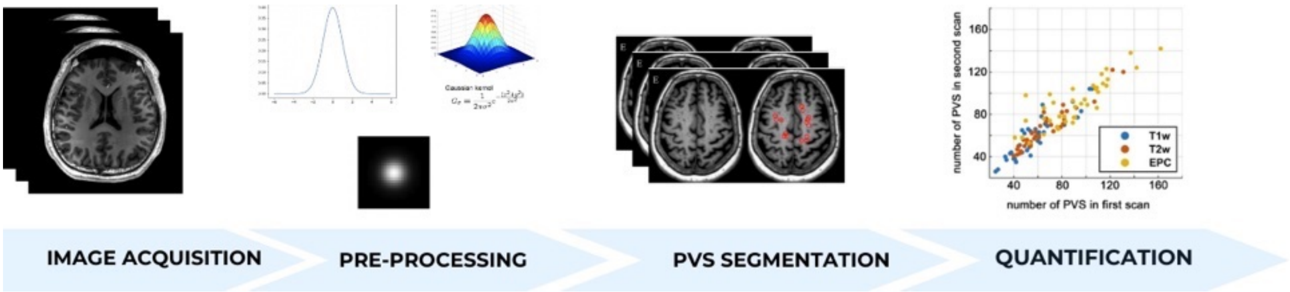

Figure 2.7: General workflow for quantifying PVS in brain MRI scans.

- *Imaging acquisition:* The visibility of PVS is closely related to the imaging technique. In particular, MRI is significantly affected by both magnetic field strength and image resolution. Higher field strengths provide grater detail and ensure the visualization of small structures, but their availability is limited making it difficult to build large datasets. Therefore, MRI scans acquired with 1.5 and 3 Tesla have been more widely used both in research and clinical practice. High-quality brain MRI sequences, particularly T1-weighted, T2-weighted and FLAIR, are critical for accurate analysis. Among these, T2-weighted images should be preferred because PVS appear hyperintense (brighter) making them easier to recognize (Kwee and Kwee, 2007). However, some studies have combined multiple MRI acquisition modalities improving the distinction between PVS from other brain structures (Sepehrband et al., 2019).

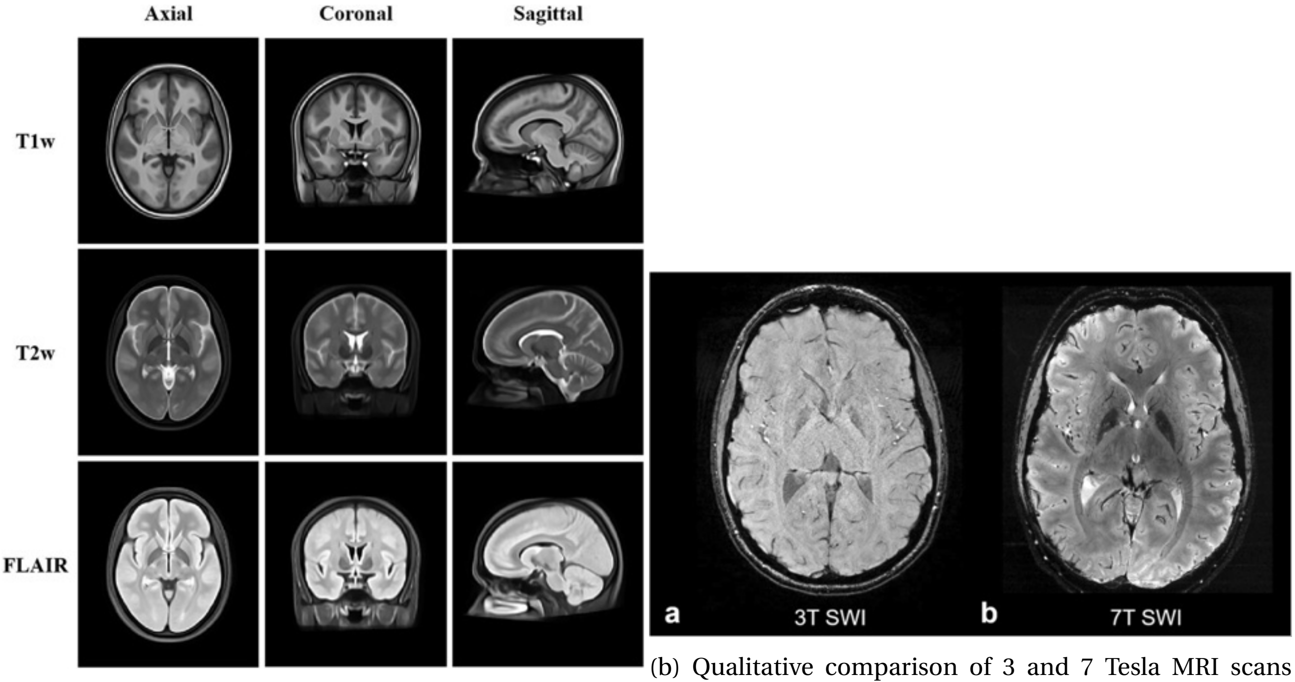

(a) MRI's types (Shah et al., 2023).

(b) Qualitative comparison of 3 and 7 Tesla MRI scans (Vachha and Huang, 2021).

Figure 2.8: Magnetic field strength types (left) and corresponding image resolutions (right) used in brain MRI for PVS detection.

- *Preprocessing of MRI:* Preprocessing steps, including noise reduction, bias field correction and co-registration of images from different modalities, are essential to improve the clarity and consistency of MRI data. This step ensures valid and mutually comparable MRI data for subsequent steps.
- *PVS detection and segmentation:* There are mainly two approaches for detecting and segmenting PVS: the classical or manual approach and the automatic one. The former relies on predefined visual rating

scales such as the Wardlaw or Potters scale, strictly human-related since human evaluation is required to classify or score the PVS based on size, number or distribution within certain brain regions. The latter, instead, allows to recognize more PVS candidates by implementing filters or convolutional neural networks such as U-Net. In recent years, semi-automated techniques have also adopted.

- *Quantification of PVS:* After segmentation, region of interest (ROI) analysis is performed to quantify PVS in specific brain regions, such as the basal ganglia or white matter. The volume or number of PVS in each ROI is calculated. In semi-automated methods, this stage may involve manual correction to address noisy labels or mislabeled regions from the automated algorithms.

Existing techniques for quantifying MRI-visible perivascular spaces

Several techniques have been developed to quantify MRI-visible PVS, each with different levels of complexity, accuracy and automation. Broadly speaking, we can divide these methods into manual and automated techniques (Figure 2.9).

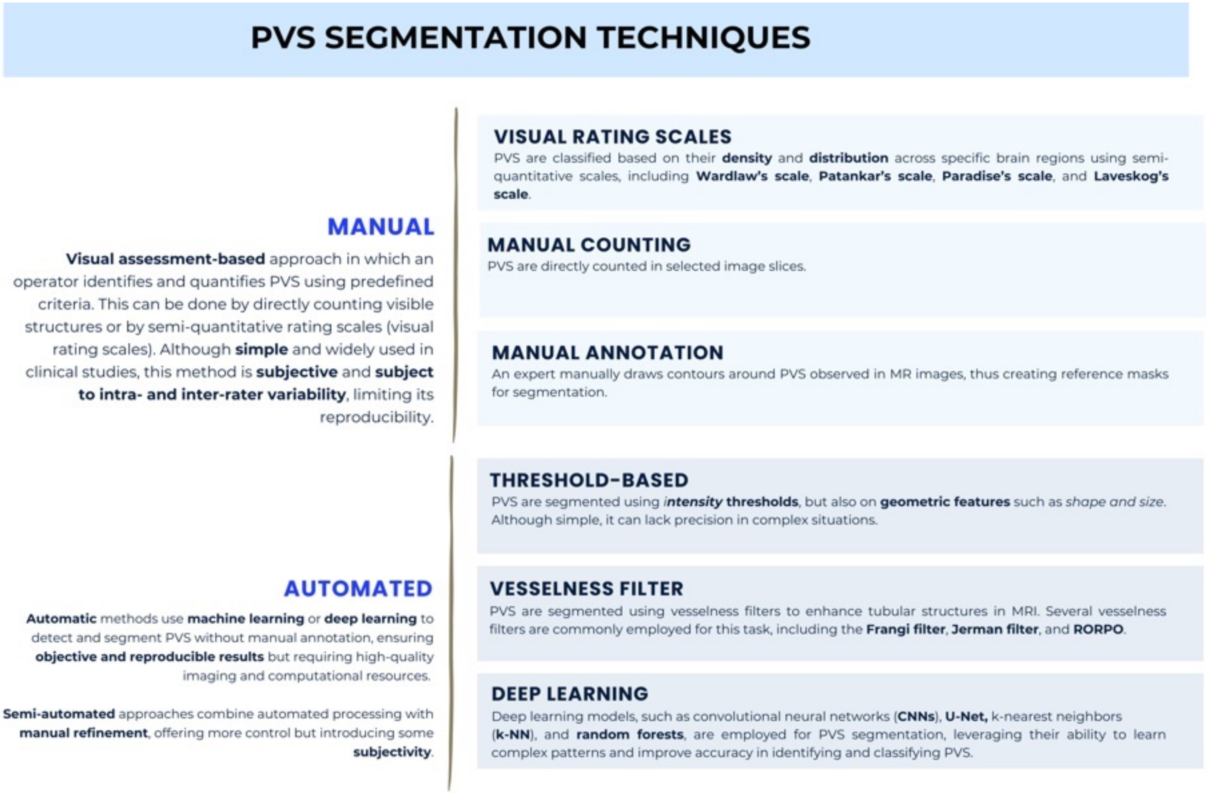

PVS SEGMENTATION TECHNIQUES

MANUAL

Visual assessment-based approach in which an operator identifies and quantifies PVS using predefined criteria. This can be done by directly counting visible structures or by semi-quantitative rating scales (visual rating scales). Although **simple** and widely used in clinical studies, this method is **subjective** and **subject to intra- and inter-rater variability**, limiting its reproducibility.

VISUAL RATING SCALES

PVS are classified based on their **density** and **distribution** across specific brain regions using semi-quantitative scales, including **Wardlaw's scale**, **Patankar's scale**, **Paradise's scale**, and **Laveskog's scale**.

MANUAL COUNTING

PVS are directly counted in selected image slices.

MANUAL ANNOTATION

An expert manually draws contours around PVS observed in MR images, thus creating reference masks for segmentation.

AUTOMATED

Automatic methods use **machine learning** or **deep learning** to detect and segment PVS without manual annotation, ensuring **objective and reproducible results** but requiring high-quality imaging and computational resources.

Semi-automated approaches combine automated processing with **manual refinement**, offering more control but introducing some **subjectivity**.

THRESHOLD-BASED

PVS are segmented using ***intensity* thresholds**, but also on **geometric features** such as *shape and size*. Although simple, it can lack precision in complex situations.

VESSELNESS FILTER

PVS are segmented using vesselness filters to enhance tubular structures in MRI. Several vesselness filters are commonly employed for this task, including the **Frangi filter**, **Jerman filter**, and **RORPO**.

DEEP LEARNING

Deep learning models, such as convolutional neural networks (**CNNs**), **U-Net,** k-nearest neighbors (**k-NN**), and **random forests**, are employed for PVS segmentation, leveraging their ability to learn complex patterns and improve accuracy in identifying and classifying PVS.

Figure 2.9: Existing techniques for quantifying PVS.

Manual segmentation Visual rating scales are among the earliest and most common manual methods used to assess PVS in brain MRI scans. These scales provide a standardized way to estimate the severity or burden of PVS by evaluating criteria such as the number, size and distribution of PVS in specific brain regions such as the basal ganglia, white matter and hippocampus. Severity indicates the PVS burden. PVS burden consists of both the number of PVS and their size. A grater burden means there are more unusually large PVS. In healthy individuals, PVS are typically small and few in number (typically smaller than 3mm (Wardlaw et al., 2020)). However, when they become more numerous or enlarged, they can indicate underlying conditions, such as small vessel disease, neurovascular disorders, inflammation or aging-related changes. Typically, high PVS severity values (Figure 2.10) are related to neurological conditions, such as cognitive decline Shen et al. (2021). Additionally, in neurodegenerative diseases such as Huntington's disease (Chan et al., 2021), it may increase with disease severity. Several visual rating scales have been used for this purpose, including those of Patankar et al. (2005), Laveskog et al. (2018) and Paradise et al. (2020). The most widely used is certainly the Wardlaw's scale (Potter et al., 2015), which is also often used in clinical

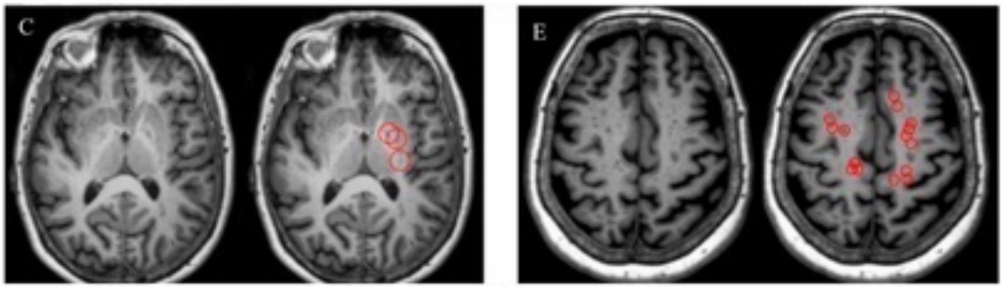

Figure 2.10: C. An example of ambiguous BG PVS. The three identified PVS circled. E. An example of severe CSO PVS pathology, with 15 PVS circled (Paradise et al., 2020).

studies of PVS. This method involves manually counting PVS on selected slices in specific brain regions: CSO, BG and midbrain. Based on the slice with the highest visually assessed PVS, the scan is rated using a simple scoring system. In the case of the basal ganglia and centrum semiovale, we are considering a 5-point scale[3]: 0 (no PVS) to 4 (severe PVS burden) which is often simplified for the midbrain to a 2-point scale: 0 (no visible), 1 (visible). The scale allows for a specific assessment of PVS by region. Karkoska et al. (2024) adopted a visual-rating scale approach in order to study dilated PVS in children with sickle cell disease following the international consensus STandards for ReportIng Vascular changes on nEuroimaging (STRIVE) criteria for defining dPVS. They rated dilated PVS on an ordinal scale in the BG and CSO from 0 (none) to 4 (>40 dilated PVS) and in the midbrain as 0 (absent) or 1 (present). Although visual rating scales provide a straightforward way to assess PVS by assigning severity scores based on their count, this approach does not allow for more detailed analysis. First, manual segmentation is extremely time-consuming. Each PVS is very small, usually less than 5 mm³ in volume, but the total PVS volume in a young, healthy person can average around 5000 mm³ (Pham et al., 2022). Considering the resolution of modern MRI scans, where each voxel represents 1 mm³, manually labeling around 5000 individual voxels would be required to map the PVS in just one person. This is an incredibly slow and tedious process. Additionally, there is a large risk for detection bias: Wardlaw's scale, for instance, has limitations when facing significant asymmetries in PVS distribution between the brain's hemispheres. In such cases, the scale specifically targets the analysis to the hemisphere with the highest PVS count, potentially missing critical information about the underlying pathology (Jiang et al., 2022). Furthermore, the ability to visualize PVS strictly relies on MRI resolution. Lower-resolution images can make these detection methods ineffective, making it difficult or impossible to accurately calculate the number PVS. Manual segmentation also fails to provide insights into the volume of PVS, which is particularly important for evaluating neurodegenerative diseases. Another limitation is that longitudinal studies of PVS are challenging. The grading scales used are too coarse to detect changes over time, which limits their use to cross-sectional studies. Despite these disadvantages, manual segmentation remains essential as the gold standard for the development and validation of automated algorithms aimed at detecting and measuring PVS more efficiently.

Automated segmentation Several automated and semi-automated detection methods have been developed to overcome the limitations of traditional manual approaches. These advanced techniques are gaining importance due to their ability to learn complex features associated with PVS and accurately detect them. Based on the existing approaches, we can categorize these approaches into two main groups: classical image processing techniques and AI-based techniques.

CLASSICAL IMAGE PROCESSING Classical image preprocessing techniques refer to traditional image analysis methods used to detect PVS based on prior features such as shape, size or voxel intensity (Boespflug et al., 2018). These methods are affected by noise and require careful tuning to achieve optimal results, so in recent years, classical image processing techniques are often combined with more advanced techniques such as machine learning models with the aim of improving data quality and emphasizing relevant features to facilitate segmentation and classification. The naturally low intensity of PVS with respect to

---

[3] 0: No visible PVS; 1: Few PVS (1-10 visible); 2: Mild PVS (11-20 visible); 3: Moderate PVS (21-40 visible); 4: Severe PVS (>40 visible)

other brain issues in MRI has allowed the evolution of a simple metric for PVS detection: intensity threshold. This method involves defining a threshold or range of intensities in the MRI images that corresponds to PVS, differentiating them from the surrounding brain tissue. By isolating voxels (the 3D equivalent of pixels in medical imaging) that match this intensity range, the algorithm can identify regions that are likely to be PVS. The resulting image is a binary map where all voxels above the threshold are set to 1 (white) and all voxels below the threshold are set to 0 (black). There are two possible types of thresholds: global and local thresholds. Global thresholds are fixed thresholds for the entire image, while adaptive thresholds vary locally, adjusting for changes in intensity in the image. Several studies have relied on intensity thresholding. (Ramirez et al., 2011), for example, adapted the software "Lesion Explorer", originally designed to exclude PVSs from analysis, to identify them using intensity thresholds. (Boespflug et al., 2018), instead, implemented a fully automated algorithm, Multimodal Autoidentification of Perivascular Spaces (MAPS), identifying PVS by analyzing features such as their intensity relative to surrounding voxels, cluster size and linearity. The algorithm was able to visualize the distribution of PVS in 3D, making it more effective for detecting subtle longitudinal changes in PVS over time. However, to analyze the intensity and visually confirm the detection of PVS, two MRI sequences (T1w and FLAIR) were needed. In general, this approach is computationally efficient and easy to implement. However, the resulting binary map is highly sensitive to the choice of thresholds and different MRI machines or settings may result in variable intensity ranges. In addition, this approach is highly limited to the assessment of PVS in white matter, as it relies heavily on local intensity contrasts, which are less pronounced in other brain regions. Another valid approach to PVS detection and segmentation is the application of vesselness filters. Vesselness filters are designed to enhance tubular or vessel-like structures in medical images. The PVS are often elongated and vessel-like in appearance, making vesselness filters particularly suited for their detection. A widely used filter for PVS detection is the Frangi filter (Frangi et al., 1998). This mathematical approach guarantees the detection of elongated structures in MRI images by analyzing the local intensity variations in them. The intensity variation is described by the combination of the three eigenvalues $\lambda_1, \lambda_2, \lambda_3$ of the local Hessian matrix. By analyzing this combination, the filter highlights regions that resemble tubular structures by reducing the noise present. Basically, regions where two eigenvalues are small and one is large in magnitude are possible PVS candidates. This filter is typically applied at multiple scales, allowing the detection of structures of varying size. It is very sensitive to noise, affecting the detection of low-intensity PVS. The Jerman Filter (Jerman et al., 2015), a Hessian-based filter similar to the Frangi filter, addresses the challenge of detecting low-intensity and variable-intensity regions by modifying the vesselness computation. It incorporates contrast normalization into the magnitude of the eigenvalues, helping mitigating the effect of contrast changes and improving the detection of low-intensity structures. However, achieving better performance requires a deeper fine-tuning of parameters. Finally, another valis filter is RORPO (Robust Optimally Oriented Flux) Filter. This filter aims at detecting tubular structures by focusing on the directional flux across multiple orientations without relying on the Hessian matrix. It evaluates the gradient change in several oriented directions around each voxel and observes the consistency of intensity variations across them. In such way, the filter is more robust to both PVS size and imaging noise and artifacts, allowing for detecting vesselness with different orientations and complex shapes. However, it is more memory-consuming and time-consuming with respect to the previous filters. In general, the choice of filter depends on the desired balance between sensitivity and specificity: Frangi and Jerman prioritize a higher number of true positives, risking more false positives, while RORPO favors a lower number of false positives at the expense of sensitivity. Hessian-based filters, such as Frangi and Jerman, suffer from poorer PVS localization due to pre-smoothing, which leads to errors with larger or more closely spaced PVSs. RORPO, however, struggles with anisotropic voxels due to its assumption of uniform voxel spacing (Bernal et al., 2022).

MACHINE AND DEEP LEARNING With the advent of machine learning, automated approaches for PVS detection and segmentation have been increasingly applied in medical imaging. These methods are particularly effective because they can learn and recognize complex patterns and features within the input data difficult to detect using traditional methods. The main machine and deep learning models that have been applied to PVS segmentation task are random forests and convolutional neural networks (Pham et al., 2022). Among these, the so called U-Net (Ronneberger et al., 2015) model, have emerged as the most effective method for PVS segmentation but the first instance of learning-based approach in PVS segmentation relies on a random forest model described by Park et al. (2016). The model accepted labels directly obtained from Frangi filter and refined manually. Haar-like features normalized with respect to the principal directions of the underlying image derivatives, have been extracted in order to train the classifier (Park et al., 2016). Also

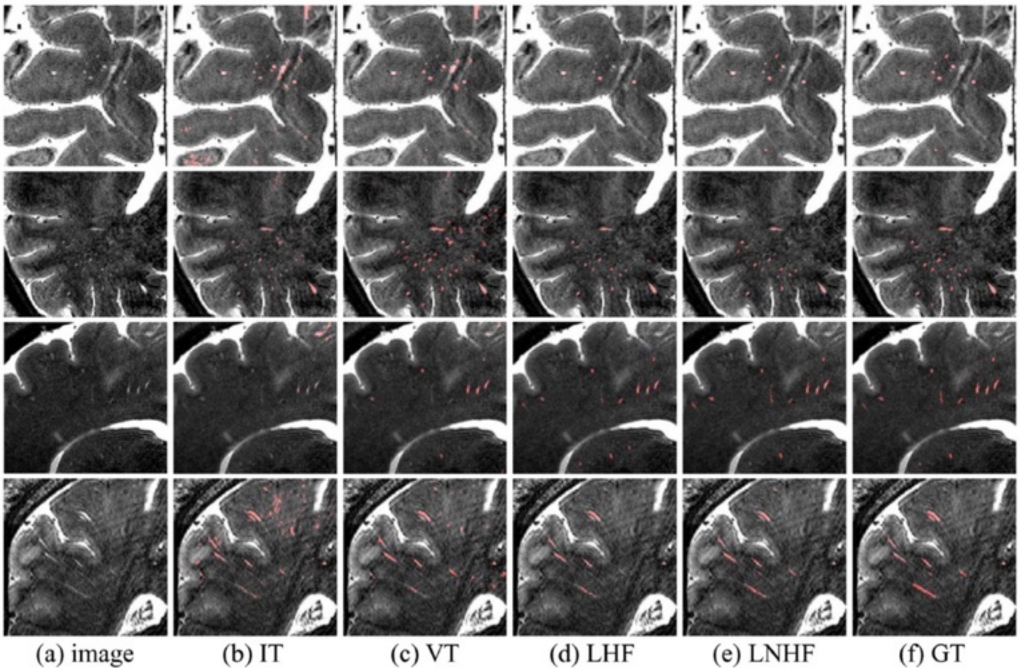

Figure 2.11: Visual comparison between normalized Haar features (LNHF), the method using simple intensity thresholding (IT), the method using vesselness thresholding (VT) and the learning-based method using the conventional Haar features (LHF). Last column represents the ground truth (GT). (Park et al., 2016)

recent studies have highlighted the versatility and effectiveness of convolutional neural networks, particularly the U-Net model, in PVS segmentation. The U-Net model (Ronneberger et al., 2015) is designed for semantic segmentation, characterized by its U-shape as represents in Figure 2.12. Its shape coming from two main components: an encoder and a decoder. The former consists of a path where the size of the image progressively reduces in order to extract as much relevant features as possible. In practice, at each level two 3x3 convolutions, an activation function and max pooling have been performed on increasing number of channels. By doubling the channels we can capture complex details. The decoder, known as expansion path, instead, aims at restoring features to their original image size including, at each level upsampling operations. A distinctive characteristic of the model is the use of skip connections: connections that directly concatenate the features in the encoder with the corresponding features in the decoder, acting as finest details for improving the segmentation. At the end of the decoder the label map is obtained by a 1x1 convolution, which classified each pixel according to its class. The entire network is designed to exploit both global context and local details, allowing for a high accurate PVS detection in complex environments, where PVS size and intensity is always changing. One of the first studies where convolutional neural networks were used for PVS quantification was conducted by Dubost et al. (2019a), who introduced a regression method to detect PVS in the BG, resulting in a high intra-class correlation coefficient (ICC) of 0.74. A subsequent improved network (Dubost et al., 2019b) allowed for quantifying PVS across multiple brain regions, including the midbrain, hippocampi, basal ganglia and centrum semiovale. Boutinaud et al. (2021), on the other hand, proposed a deep learning model consisting in the combination of two models: a convolutional autoencoder and a U-Net architecture. The study focused on the 3D segmentation of the PVS in BG. Trained on T1-weighted MRI of a large cohort of 1,832 healthy young adults, the model effectively segmented the PVS, performing well especially in detecting larger PVS clusters. Specifically, after a pre-processing phase of the MRI scans, the autoencoder was trained on unannotated volumes to capture useful representations of the data, which consisted of the initial weights for U-Net training. The skipped connections, therefore, allowed for accurate PVS detection. Similarly, Rashid et al. (2023) adapted a lightweight and effective U-Net model for the detection of PVS, with which different combinations of MRI sequence acquisition techniques, such as SWI, FLAIR, T1-weighted and T2-weighted, were studied. The model was designed in a scalable man-

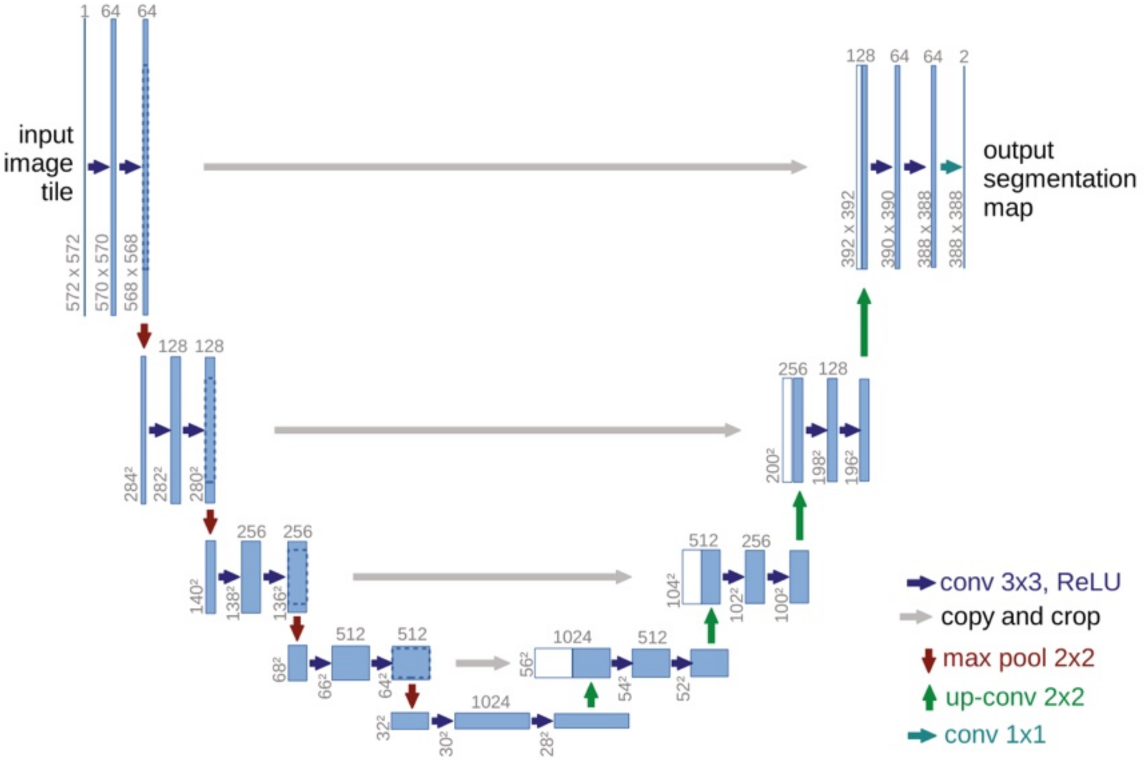

Figure 2.12: Basic U-Net model rappresentation (Pham et al., 2022).

ner: the network can easily be expanded to include multiple sequences, becoming a multi-channel model (Rashid et al., 2023). The network not only efficiently predicted PVS from MRI scans, but also highlighted the critical role of T2-weighted MRI for accurate detection. Furthermore, the model was able to generate complete brain maps of PVS, unlike traditional methods based on ratings or filters, which typically focus on limited brain regions.

Deep learning in Parkinson-related studies Up to date, the application of deep learning has significantly improved clinical research allowing correlations between different imaging features and clinical factors to be identified. In the context of PVS detection, numerous studies have applied machine learning techniques to correlate PVS enlargement with cognitive decline or specific clinical variables. A remarkable example is the mcPVS-Net developed by Huang et al. (2024), which allowed an in-depth analysis of the relationship between PVS volume and clinical variables such as age, hypertension and WMH. However, the detection of PVS in Parkinson's disease patients is still at an early stage. A noteworthy study in this area is that of Cai et al. (2024), who developed an effective deep learning method to segment PVS in a cohort of Parkinson's patients. The study was notable for its focus on replicability and accessibility, leveraging on T2-weighted 3 Tesla MRI images of approximately 20 adults. The proposed method is based on a multiscale supervised nested dense attention network, which facilitates the interplay between high and low-level image features, allowing segmentation of PVS with a valid DSC of 0.70.

Chapter 3

Data

3.1 Study participants

The data used during the study was a dataset made of neurological data obtained from 47 adult participants diagnosed with PD. This dataset specifically includes individuals affected by PD who do not have concurrent brain injury or focal WM hyperintensity. This inclusion criterion was carefully selected to minimize noise factors that could potentially alter PVS segmentation. Due to incomplete data acquisition during the T1 time point, one subject has been excluded from the dataset. An additional participant who failed MRI linear registration due to acquisition-related issues were excluded, resulting in a total of 47 subjects.

Time point	#Subjects	#Scans
T0	49	49
T1	48	48
TOT	47[1]	94[2]

Table 3.1: Dataset composition, including the number of subjects and the scans obtained for each time point.

Sex	#Subjects	Age, years, mean
Men	25	67.4
Women	22	63.0

Table 3.2: Characteristics of study population

3.2 Data acquisition

MRI images data were acquired with a 1.5 Tesla Magnetom Aera scanner (Siemens; Erlangen, Germany), equipped with a 12-element designed head matrix coil. MRI anatomical protocol included the following sequence: 3D-MPRAGE T1-weighted (repetition time [TR] = 1750 msec, echo time [TE] = 3.15 msec, inversion time [TI] = 1000 msec, flip angle = 8°, matrix = 256 × 256, NEX = 2, field of view [FOV] = 25 x 25 cm, voxel size = 1 x 1 x 1 mm, acceleration factor PE = 2).

MRI scans were acquired for each participant at two distinct time point, separated by an interval of approximately one month. The first acquisition, referred to as T0, represented the initial baseline scan, whereas the second acquisition, T1, serves as the follow-up. This longitudinal approach is conceived for a detailed analysis of temporal changes occurring within the brain over the given period.

An expert neuroradiologist (20 years of experience) examined all MRIs to exclude the presence of concomitant brain lesions and focal white matter hyperintensities according to the Fazekas scale.

---

[2] Total number of subjects included in the study, excluding incomplete and invalid data.

[2] Total number of MRI scans included in the study, excluding incomplete and invalid data.

Sequence	Acquisition method	Field of view [mm]	Slices	Acquired resolution [mm]	TR/TE/TI [ms]
T1-w	3D MPRAGE	256 × 256	160	1 × 1 × 1	1750/3.15/1000

Table 3.3: Parameters of the T1-weighted MRI sequences used for the segmentation of normal-appearing and pathological brain regions.

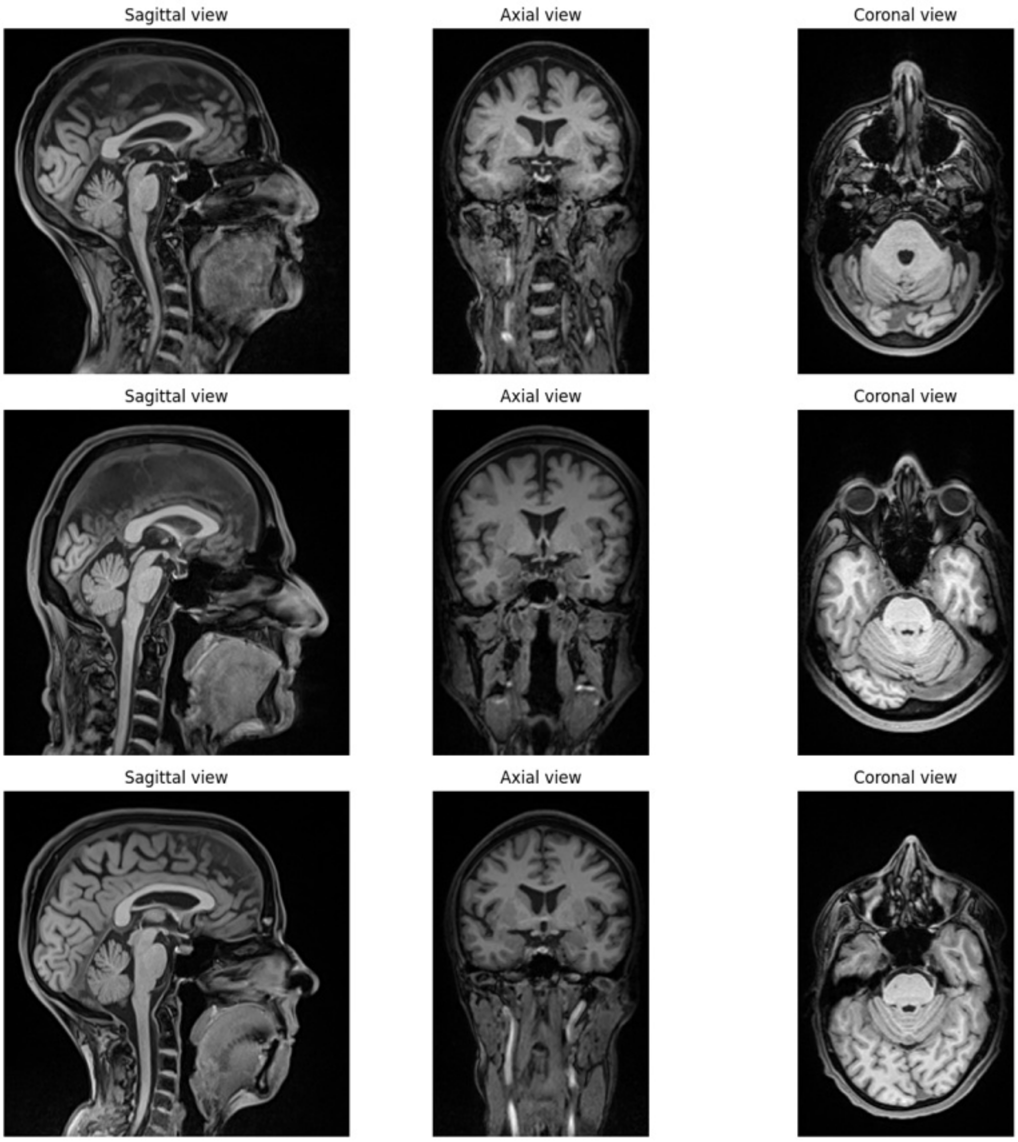

Figure 3.1: MRI scans from different subjects, displaying slices from the three axial views of their brain: sagittal, axial and coronal perspectives.

3.3 Ethical considerations

The study was designed as a prospective case-control investigation and received approval from the Ethical Committee of Fondazione Policlinico Universitario Campus Bio-Medico (N. SC 2022.086).

Written informed consent was obtained from all participants prior to their involvement, ensuring their understanding and voluntary participation.

Chapter 4

Materials and methodology

The primary objective of this project was to automatically detect and segment PVS from MRI data.

Due to the lack of a valid ground truth and the considerable time cost required to produce manual annotations, a semi-automatic annotation procedure was necessary. To achieve this, we enhance the visibility of potential PVS structures in WM through classical image processing and refined their delineation based on neuroradiologist feedback. This process was crucial to properly train the neural network.

4.1 Data preparation

Selecting data is crucial to accurately segment PVS, as the quality, intensity and type of images significantly impact the performance of the detection methods. Thus, in order to correctly detect the PVS and ensure standardized and high-quality input for further analysis, an modular image pre-processing pipeline has been performed.

Based on existing literature, PVS are predominantly found in the WM of the brain. As a result, our study specifically targets this region by isolating it from the MRI scans. To ensure that only comparable brain tissue is included in the analysis, non-brain structures were removed and spatially aligned to a shared reference space by using an average template. This alignment process was necessary to ensure consistency across all subjects. To minimize variability across subjects, instead, intensity normalization was applied. All pre-processing was performed using FSL (FMRIB Software Library).

The data preparation pipeline involved several steps, as represents in Figure 4.1:

1. DICOM to NIfTI conversion
2. Skull stripping
3. Computation of an average template
4. Linear registration to the average template
5. WM extraction

Step 1: DICOM to NIfTI conversion

T1-weighted MRI scans were initially stored in DICOM (Digital Imaging and Communications in Medicine) format. This format is the standard in storing medical images such as MRI, TAC or RX. This is a very rich information data type, it contains the 3D image data but also the acquisition parameters, machine information, patient information and hospital information. The extension of the file is .dcm. The image volume is divided into single slices, each stored as DICOM files. This format contains a lot of information but does not allow to store the entire volume in a unique file, which, instead, is made possible by the NIfTI format. NIfTI (Neuroimaging Informatics Technology Initiative) is a specific format for medical imaging widely used in neuroimaging when dealing with particular images such as MRI, fMRI or DTI which stores entire volumes in 3D or 4D single files. The conversion from DICOM to NIfTI file is then suggested in order to make the imaging analysis and comparison easier, in particular when dealing with automated analysis.

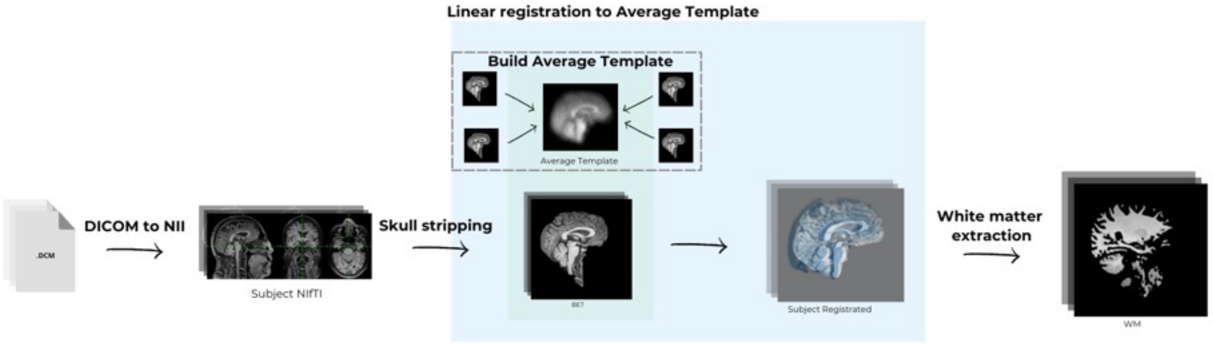

Figure 4.1: Data preparation pipeline.

We converted DICOM to compressed NIfTI (.nii.gz) using `dcm2niix`, the most widely used method that guarantees the preservation of metadata:

```
dcm2niix -o <output_directory>
         -z y <input_dicom_folder>
```

where `-z y` enables gzip compression.

Step 2: Skull stripping

Skull-stripping, commonly referred to as brain extraction, consists in removing non-brain tissue from MRI scans and isolating only the brain information. Skull stripping is a fundamental step in neuroimaging, as it helps anonymize the brain scans by removing identifying anatomical features and reduces the potential effect of noise in following studies.

Several software tools have implemented skull-stripping algorithm, such as FSL (Jenkinson et al., 2012), ANTs (Avants et al., 2011) and FreeSurfer (Fischl, 2012). For this study, the FSL Brain Extraction Tool (BET) has been chosen due to its reliability and efficiency in isolating brain tissue:

```
bet <input_image> <output_brain> -f 0.7 -R -m
```

where:

- `-f 0.7` controls the aggressiveness of skull stripping (Fractional Intensity Threshold). A higher value results in a smaller brain mask.
- `-R` enables robust brain center estimation, which can improve extraction in cases where the head position varies.
- `-m` generates a binary brain mask alongside the extracted brain image. The mask can be used for further processing or masking other images.

Step 3: Computation of average template

An average template was created as reference space for standardizing spatial alignment across multiple subject scans. This process results in decreasing inter-subject variability and facilitating the comparison of structural features across subjects in the following studies.

Firstly, all subject-specific NIfTI files have been merged in a single 4D file using the ‘fslmerge‘ command from the FSL suite, which concatenates 3D scans along the temporal dimension. Specifically, we represented al subject scans in a single data structure through the following command:

```
fslmerge -t <output_4d_file> <list_of_input_files>
```

where `-t` option specifies the axis of concatenation, in our case the time axis.

Once the 4D file has been generated, the mean was calculated using the ‘fslmaths‘ command specifying ‘-Tmean‘ parameter:

```
fslmaths <input_4d_file> -Tmean <output_average_template>
```

where `-Tmean` parameter computes the average intensity at each voxel across all time points, resulting in a 3D template capturing the average anatomical structure shared by all subject.

Step 4: Linear registration to average template

Each subject’s MRI was linearly registered to the computed template using FSL’s `FLIRT` (FMRIB’s Linear Image Registration Tool):

```
flirt -in <input_image>
      -ref <template_image>
      -out <output_image>
      -omat <transformation_matrix>
```

where:

- `<input_image>` is the individual subject’s T1-weighted scan,
- `<template_image>` is the computed average template,
- `<output_image>` is the registered output,
- `<transformation_matrix>` stores the transformation parameters.

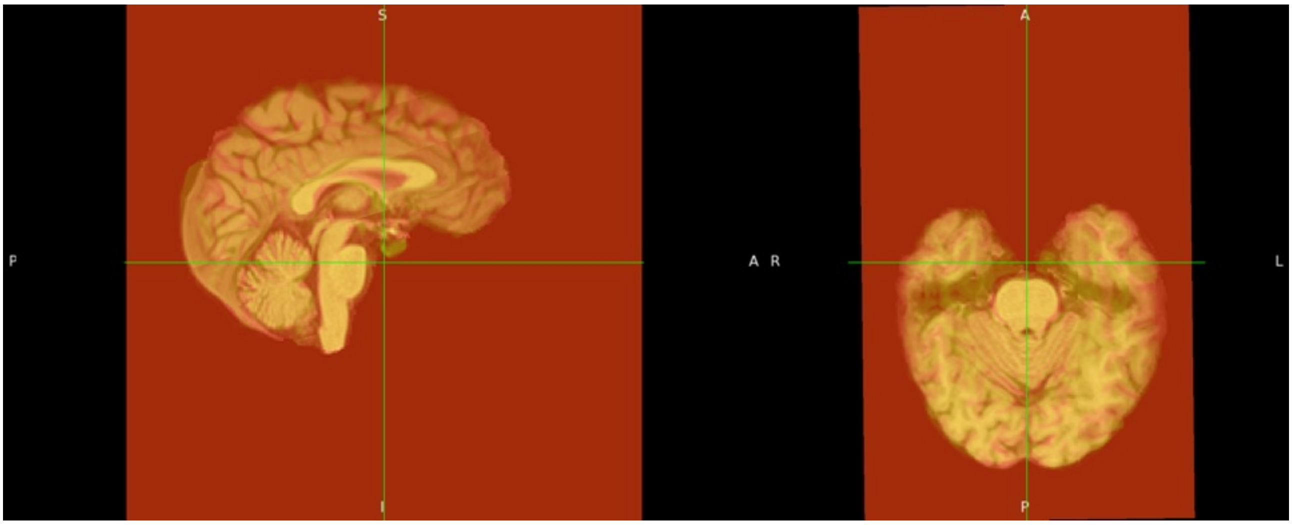

Figure 4.2: Overlay of two registered brain to the average template in sagittal view (left) and axial view (right).

Step 5: White matter extraction

Given that PVS are predominantly located within the WM area of the brain, our segmentation approach specifically targets this ROI. Extracting the WM allows us to remove non-relevant brain tissue, which could introduce noise and negatively impact segmentation accuracy.

To achieve this, we used FSL-FAST, a widely used tool for automated brain tissue classification. The algorithm segments the brain into three primary tissue types: gray matter, white matter and cerebrospinal fluid, producing partial volume estimation (PVE) maps as output. The command used for this step is as follows:

```
fast -t 1
     -n 3
     -o <output_prefix> <input_brain_image>
```

where:

- `-n 3` specifies the number of tissue types to be classified during the segmentation process. In this case, the algorithm distinguishes between three main tissue classes: CSF, GM and WM (Figure 4.3).
- `-t 1` indicates the type of MRI scan being processed. In this case, the value `1` corresponds to a T1-weighted MRI scan.

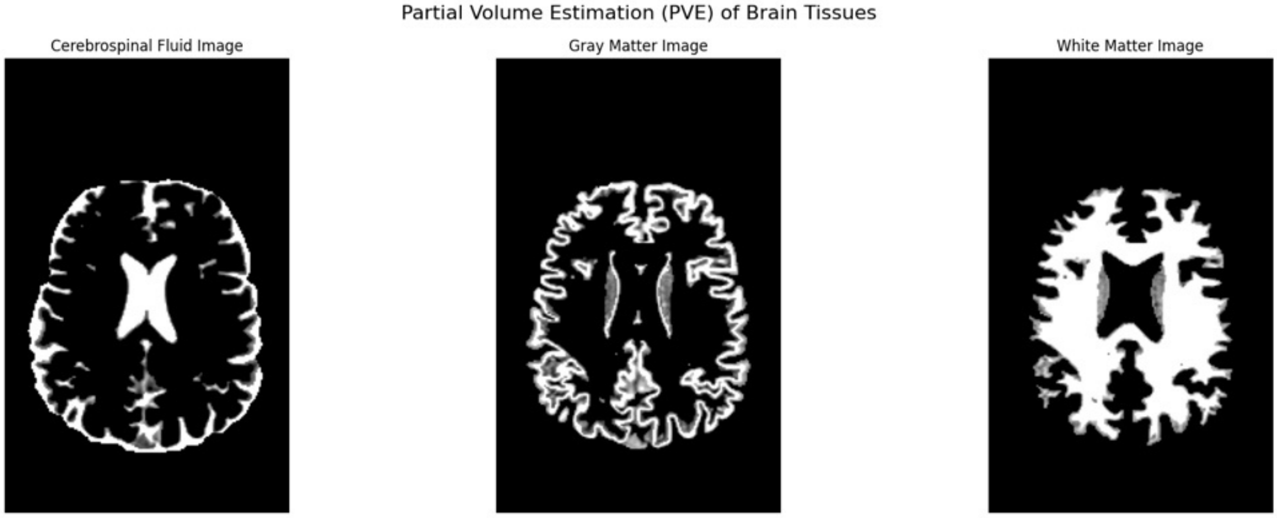

Figure 4.3: Partial volume estimation of the brain tissues.

Once obtained the partial volume estimation mask of the WM, we isolated the WM tissue by applying a thresholding and binarization process. This step ensures that only voxels with a probability of being classified as WM above a certain threshold were included, minimizing the inclusion of misclassified regions. Based on a qualitative analysis and subsequent expert validation, we determined that the optimal probability threshold for WM extraction is 0.5. In Figure 4.4 are represented the resulting binary WM segmentation across different threshold values. As observed, using restrictive thresholds, such as 0.7 or 0.9, leads to exclude relevant areas of WM. Conversely, lower threshold values tend to introduce noise in the segmentation, incorrectly segmenting different areas such as GM or CSF. Threshold value equal to 0.5, instead, balances the accuracy in boundaries delineation and noise inclusion. The WM binarization process inadvertently removed some voxels classified as GM or CSF due to their lower intensity values. In particular, this process removed some of the PVS present within the WM: those that were particularly clearly recognizable even by the naked eye. This process would have led to the loss of relevant information and would have altered the subsequent detection of PVS. Therefore, to address this issue, we applied some morphological operations under the name of dilation techniques (Figure 4.5). Specifically, we filled the black holes in the WM boundaries using a hole-filling function and completed the object area by applying the binary-closure function. This step allowed us to generate a more complete WM mask. The effectiveness of this correction was validated by an expert neuroradiologist using FSL's fsleyes tool, confirming the accuracy of the refined WM

Figure 4.4: Binary WM segmentation across different threshold values.

segmentation.

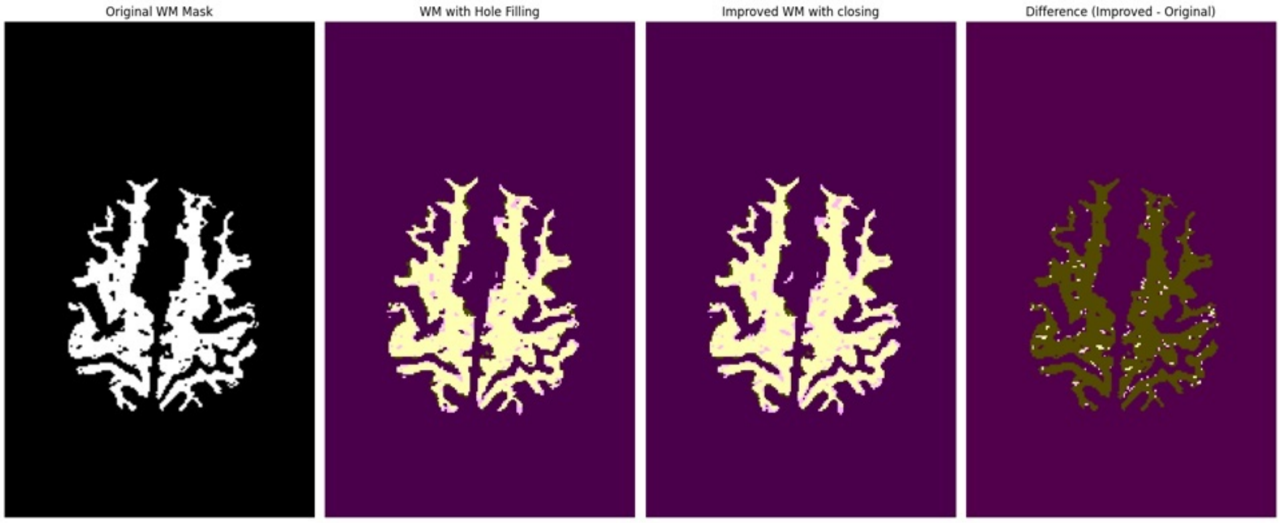

Figure 4.5: Progressive refinement of binary WM segmentation.

Once the binary WM map has been correctly generated, WM extraction has been performed by applying an element-wise multiplication between the binary map and the initial BET-processed MRI image. This operation masks the original image, preserving only the voxels corresponding to WM regions. Figure 4.6 represents the pipeline for WM segmentation.

4.2 Image-processing approach: Frangi filter-based

Over the past years, numerous studies have successfully utilized the Frangi filter to enhance vessel-like structures and generate valid segmentation maps. Research, such as Ballerini et al. (2020), Lan et al. (2023) and Dubost et al. (2019a) demonstrated the effectiveness of this technique to ensure reliable ground truth data for deep learning approaches in PVS detection.

4.2.1 Detection of perivascular spaces

Frangi filter

Frangi filter, also known as Frangi vesselness filter, is an algorithm designed for detecting tube-like structures, widely used both in 2D and 3D images. This filter, described for the first time by (Frangi et al., 1998) in 1998, is particularly effective for the segmentation of elongated structures such as blood vessels, fibers and smaller brain structures like PVS. The algorithm detects regions resembling tubes or cylinders by analyzing the local structure of an image through the mathematical concept of Hessian matrix.

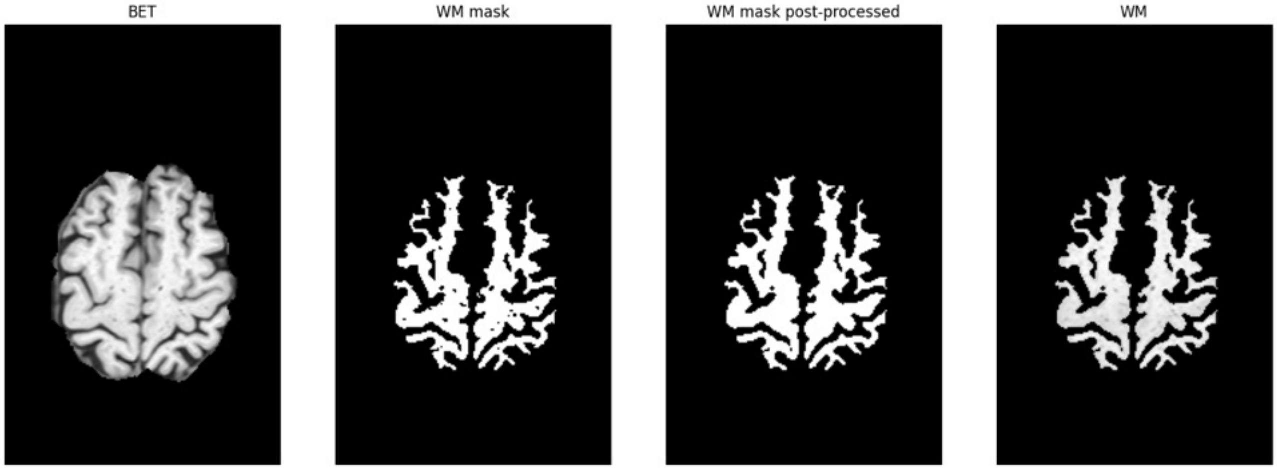

Figure 4.6: WM segmentation pipeline.

Mathematical foundations

The Hessian matrix The Hessian matrix is a square matrix composed of second-order partial derivatives of a scalar-valued function, important as is provides essential information about the local curvature of the function. In the context of image processing, the scalar function is typically the intensity function, which ensures the detection of tube-like structures.

For a 3D image, the Hessian matrix is represented as a 3 × 3 matrix of second-order partial derivatives with respect to the three spatial coordinates (x, y, z). It can be expressed as follows:

$$H = \begin{bmatrix} \frac{\partial^2 I}{\partial x^2} & \frac{\partial^2 I}{\partial x \partial y} & \frac{\partial^2 I}{\partial x \partial z} \\ \frac{\partial^2 I}{\partial y \partial x} & \frac{\partial^2 I}{\partial y^2} & \frac{\partial^2 I}{\partial y \partial z} \\ \frac{\partial^2 I}{\partial z \partial x} & \frac{\partial^2 I}{\partial z \partial y} & \frac{\partial^2 I}{\partial z^2} \end{bmatrix}$$

where:

- $I(x, y, z)$ is the intensity function of the 3D image;
- $\frac{\partial^2 I}{\partial x^2}$, $\frac{\partial^2 I}{\partial y^2}$ and $\frac{\partial^2 I}{\partial z^2}$ are the second-order derivatives with respect to the individual spatial coordinates;
- $\frac{\partial^2 I}{\partial x \partial y}$, $\frac{\partial^2 I}{\partial x \partial z}$ and $\frac{\partial^2 I}{\partial y \partial z}$ are the mixed second-order derivatives.

To compute the second-order derivatives, the image is convolved with the derivatives of a Gaussian kernel with a specific standard deviation σ. By adjusting σ we can extract structures of different sizes.

Eigenvalues and eigenvectors In mathematics, eigenvalues and eigenvectors of a square matrix A, are fundamental concepts for describing its properties.

An *eigenvector* of a square matrix A, is a non-zero vector **v** that, when multiplied by the matrix A, results in a scaled version of itself. In other words, the matrix A does not change the direction of the eigenvector, only its magnitude. Mathematically, this is represented as:

$$A\mathbf{v} = \lambda \mathbf{v}$$

where **v** is the eigenvector and λ is the eigenvalue corresponding to that eigenvector.

An *eigenvalue* λ, instead, is the scalar by which the eigenvector **v** is scaled when multiplied by the matrix A. It represents the factor by which the magnitude of the eigenvector is stretched or compressed.

For a 3D image, the Hessian matrix provides a local description of the curvature of the image at each voxel (a 3D pixel). This square matrix can be analyzed using its eigenvalues and eigenvectors. In case of Frangi filter, these eigenvalues, denoted as λ_1, λ_2andλ_3, are used to determine whether a given pixel belongs to a 'tube-like' or 'blob-like' structure. Specifically, the eigenvectors help to identify the main directions of the tubular structures and the eigenvalues indicate how sharply the image changes in those directions. A strong tube-like structure, i.e. PVS, will have one small eigenvalue (indicating little change in the direction along the vessel) and two larger eigenvalues (indicating more variation in perpendicular directions).

For each voxel, the eigenvalues corresponds to the principal curvatures of the image and the eigenvalues are sorted in ascending order, such that $|\lambda_1| \leq |\lambda_2| \leq |\lambda_3|$, where:

- λ_1 corresponds to the smallest eigenvalue, reflecting the curvature along the least curved direction.
- λ_2 and λ_3 correspond to the curvatures along the other two axes.

Vesselness probability In Frangi filter, the eigenvalues and eigenvectors are used to assess the likelihood that a given voxel corresponds to a tubular structure (Frangi et al., 1998). This likelihood is typically denoted as vesselness probability and it is computed as follows:

$$v_0(s) = \begin{cases} 0 & \text{if } \lambda_2 > 0 \text{ or } \lambda_3 > 0 \\ \left(1 - \exp\left(\frac{-R_A^2}{2\alpha^2}\right)\right) \exp\left(\frac{-R_B^2}{2\beta^2}\right) \left(1 - \exp\left(\frac{-S^2}{2\gamma^2}\right)\right) & \text{otherwise} \end{cases}$$

with:

$$R_A = \frac{|\lambda_2|}{|\lambda_3|}$$

$$R_B = \frac{|\lambda_1|}{\sqrt{|\lambda_2 \lambda_3|}}$$

$$S = \sqrt{\lambda_1^2 + \lambda_2^2 + \lambda_3^2}$$

where:

- $v_0(s)$ represents the probability that a voxel belongs to a tubular structure
- α, β, γ are predefined parameters controlling the sensitivity of the filter to the different shape measures R_A, R_B and S
- $\lambda_1, \lambda_2, \lambda_3$ are the eigenvalues of H sorted in ascending order as $|\lambda_1| < |\lambda_2| < |\lambda_3|$
- S measures vesselness contrast, highlighting intensity changes in the image
- R is the ratio of the eigenvalues, $R = \frac{\lambda_2}{\lambda_1}$, where λ_1 is the largest eigenvalue and λ_2 is the second eigenvalue. Specifically, R_A differentiates blob-like structures from plate-like and line-like structures. R_B distinguishes between plate-like and line-like structures.

The vesselness function suppress non-tube-like structures and enhances regions that resemble tubular shapes. Ideally, perfect tubular structures exhibit the following properties: $|\lambda_1| \approx 0$, $|\lambda_1| < |\lambda_2|$ and $\lambda_2 \approx \lambda_3$.

Computational core steps

Step 1: Image pre-processing In order to facilitate the PVS detection through Frangi filter, some pre-processing has been performed on the BET images. This step included:

- *Normalization:* The image intensities are scaled to ensure that they fall within a range suitable for detecting vessel-like structures.
- *Contrast enhancement:* Darker regions in the WM area has been enhanced in order to facilitate and ensure the detection of PVS.

Figure 4.7 shows the resulting image from pre-processing pipeline.

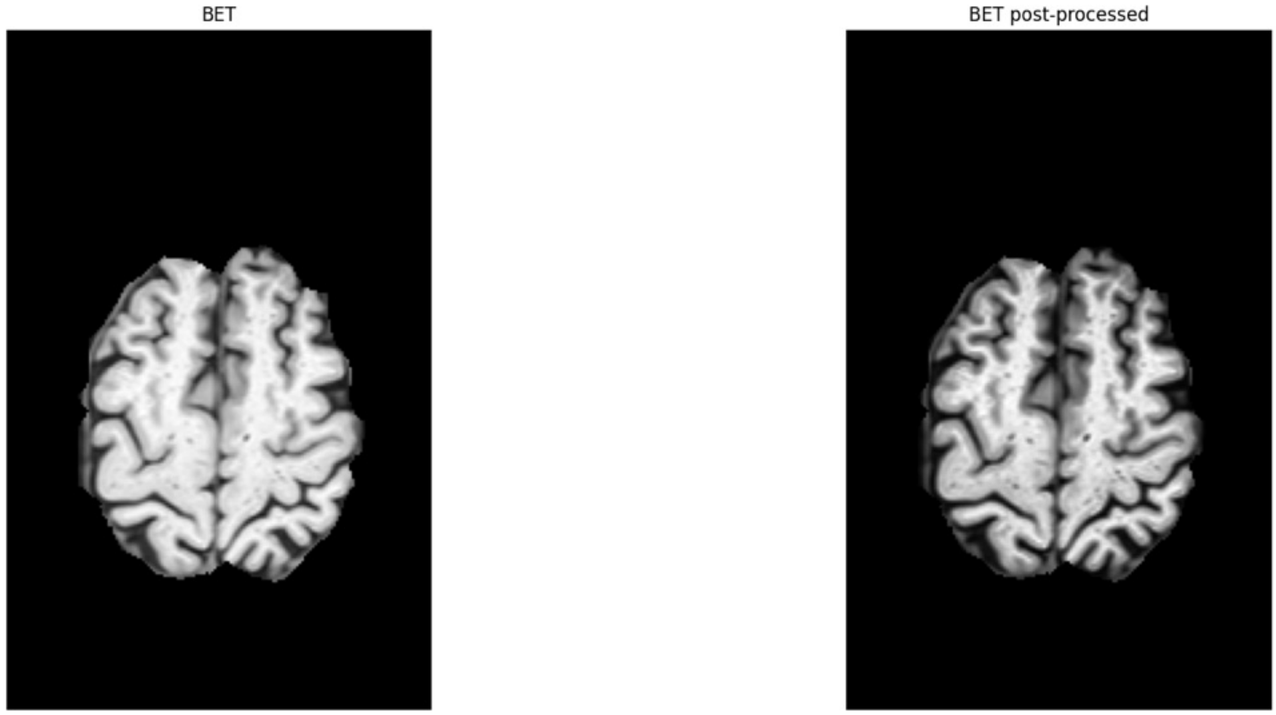

Figure 4.7: Preprocessing applied on a BET-resulting image.

Step 2: Frangi filter implementation Frangi filter is applied on the preprocessed images to highlight tubular structures. The filter works by analyzing the eigenvalues of the Hessian matrix at each voxel, computing the vesselness probability for a range of scales. The vesselness measure is evaluated at multiple scales s to accommodate vessels of varying widths.

$$V_o(\gamma) = \max_{s_{\min} \leq s \leq s_{\max}} V_o(s, \gamma)$$

where $s_{\min}$ and $s_{\max}$ define the minimum and maximum scale values according to Ballerini et al. (2018).

Frangi filter has been implemented using the QIT Module Library, a specialized software package for the visualization, exploration and analysis of neuroimaging data[1]. Initially developed for micro-structural analysis in diffusion MRI, it has been extended to various other imaging modalities, such as T1-weighted MRI. It provides computational tools for processing and visualizing imaging data along with a command-line interface tool named QIT.

In order to apply the filter, the following command has been executed:

```
qit VolumeFilterFrangi --input <preprocessed_image>
                       --output <vesselness_output>
                       --low 0.1 --high 5.0 --scales 5
                       --alpha 0.5 --beta 0.5 --gamma 500.0
                       --dark
```

where:

- `<preprocessed_image>` refers to the preprocessed MRI scan. In our case the processed BET.
- `<vesselness_output>` is the output file containing the vesselness map,
- `-low` and `-high` define the range of scales used for multi-scale filtering,
- `-scales` specifies the number of scales considered,
- `-alpha, -beta and -gamma` control the sensitivity of the filter to different structural features,

---

[1] The software is freely available for download at http://cabeen.io/qitwiki/

- `-dark` ensures the filter detects dark tubular structures. Since we were working on T1-weigthed MRIs and the PVS structures were appearing darker than the surrounding brain tissue. Hence, we imposed the condition $\lambda_2 < 0$ and $\lambda_3 < 0$ as vesselness criterion, ensuring that only dark, tube-like structures were enhanced and extracted.

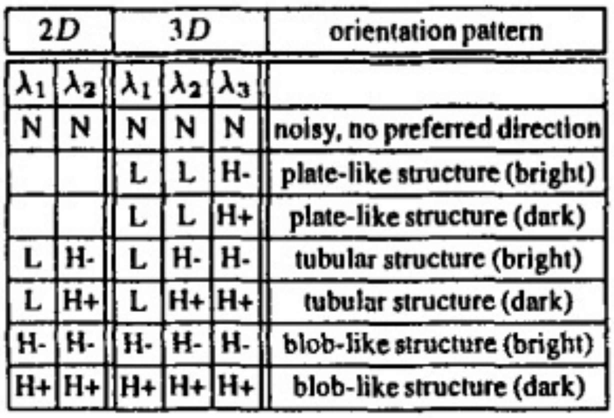

2D		3D			orientation pattern
λ_1	λ_2	λ_1	λ_2	λ_3	
N	N	N	N	N	noisy, no preferred direction
		L	L	H-	plate-like structure (bright)
		L	L	H+	plate-like structure (dark)
L	H-	L	H-	H-	tubular structure (bright)
L	H+	L	H+	H+	tubular structure (dark)
H-	H-	H-	H-	H-	blob-like structure (bright)
H+	H+	H+	H+	H+	blob-like structure (dark)

Figure 4.8: 2D and 3D possible combinations of eigenvalues to compute vesselness probability (N=noise, H=high, L=low, +/- indicates the sign of the eigenvalue) (Ballerini et al., 2018).

Frangi filter parameter selection Frangi filter is strictly correlated to several parameters which strongly influence its ability in detecting tubular structures. Different parameters should be properly tuned to accurately identify PVS while minimizing false positives.

- *Correction constants* α, β, γ: These parameters control the sensitivity of the filter in determining tube structured features in the image. Specifically:
  - α is a correction constant that controls the filter's sensitivity in deviating from a plate-like structure. When λ_1 and λ_2 are small (close to zero) and λ_3 is large, we can classify the structure as a tubular structure, 4.8. The corresponding term is:

$$\exp\left(-\frac{R_A^2}{2\alpha^2}\right), \quad R_A^2 = \frac{|\lambda_2|}{|\lambda_3|}$$

  - β is a correction constant that controls the filter's sensitivity in deviating from blob-like structures. When all the eigenvalues are large, the curve of intensity in all the three directions is high and we can classify the structure as a blob-like structure. The corresponding term is:

$$\exp\left(-\frac{R_B^2}{2\beta^2}\right), \quad R_B^2 = \frac{|\lambda_1|}{\sqrt{|\lambda_2 \cdot \lambda_3|}}$$

  - γ is the correction constant that adjusts the filter's sensitivity to areas of high variance/texture/structure. Smaller values of γ ensures the detection of low-contrast vessels. The corresponding term is:

$$1 - \exp\left(-\frac{S^2}{2\gamma^2}\right), \quad S = \sqrt{\lambda_1^2 + \lambda_2^2 + \lambda_3^2}$$

  In this study the recommended filter parameters: $\alpha = 0.5, \beta = 0.5, \gamma = 500.0$ as described from Ballerini et al. (2018) has been used.

- *Scale parameter* s: The vesselness equations 4.2.1 has been analyzed across different scales so that the filter can detect different vessels sizes. The final output of the filter, indeed, will be the maximum at scale s_i that approximately matches the size of the structure to detect 4.2.1. Usually, the chosen scale range consists in the range of structures widths. In this study, the range [0.1, 5.0] has been chosen based on previous works (Sepehrband et al. (2021), Donahue et al. (2024)).

- *Color of structure to detect*: Depending on the type of gray-scale image, the filter can detect either black ridge or white ridges. Since we are working with T1-weighted MRI, we need to specify that we are detecting darker structures.

The output of the filter is a probability map where each voxel contains the likelihood belonging to a PVS structure. A thresholding process has been performed in order to obtain valid binary maps locating the detected PVS. An intensive quantitative and qualitative analysis allowed us to choose the more appropriate threshold and filter out irrelevant regions. A in-depth statistical analysis suggested by the expert neurologist confirmed the vesselness threshold to 0.002. The results of the analysis are described in the paragraph 4.2.1.

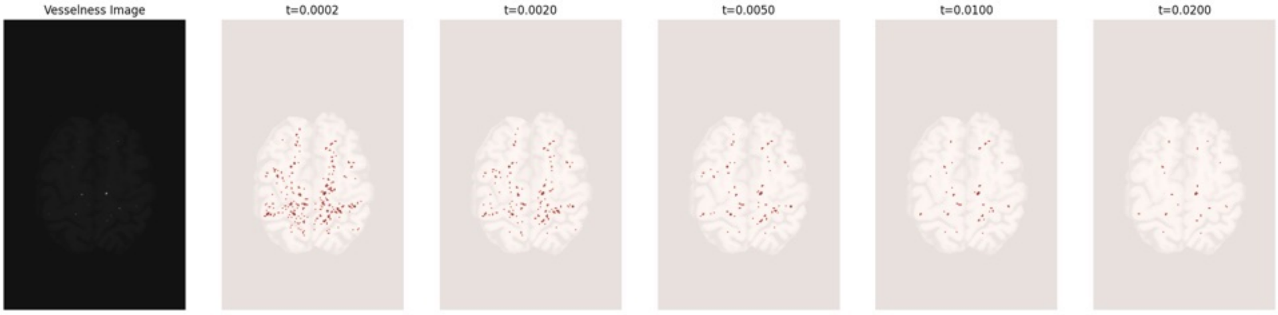

Figure 4.9: Binary vesselness map at different thresholds.

Statistical analysis for vesselness threshold selection When dealing with semi-automatic approaches based on thresholding it is crucial to carefully select the most appropriate threshold. Following the neuroradiologist's recommendation, we conducted a statistical analysis. In particular the clinician selected two thresholds that balanced the PVS segmentation accuracy and noise introduction. At this point, we analyzed the correlations between the total volume of PVS in the selected vesselness maps and several available clinical variables corresponding to PD patients. Basically, that threshold for which the total volume of PVS is more statistically correlated to the available clinical variables is the most significant. The total volume of PVS was computed as the number of voxels labeled as PVS, as described in 4.3.2.

The thresholds analyzed were 0.0002 and 0.002. The parameters for which we studied possible correlations with PVS total volume were:

- *UPDRS I, II, III*: Acronym for Unified Parkinson's Disease Rating Scale. It is a rating scale used in PD diagnosis composed of six parts. In primary stages of the disease, the first three parts are usually valuated for the disease prognosis. UPDRS I describes the mental health of the patient, including the behavior and mood in daily life such as depression or motivation. UPDRS II is an auto-evaluation of the patient regarding daily activities such as ability in speaking, writing, walking. UPDRS III is the clinical evaluation of motor abilities, valuated by experts in neurology. It includes a real valuation of patient's ability in movements;

- *SLEEP* (hours): Intended as median hours of sleep during the examined month and average hours of sleep the night before the control at T1;

- *LEDD*: Acronym for Levodopa Equivalent Daily Dose. It is referring to the levodopa equivalent daily dose, allowing comparison between different antiparkinsonian therapies.

The analysis was performed in Python, using Scipy library. According to the selected variable distributions, deeply analyzed through Shapiro-Wilk test, we performed three different statistical tests: Pearson, Spearman and, as an additional verification, Kendall Tau test. The statistical significance of the correlation was established according to the p-value, setting the statistical level of significance at 0.05. The strength of the correlation was also assessed.

4.2.2 Segmentation of perivascular spaces

In order to effectively identify individual PVS regions within brain MRI scans, connected component analysis (CCA) has been applied. CCA allowed us to deeply analyze PVS from the binary mask through relevant geometric features that provide insight into the size and shape of each identified component.

Connected component analysis

The Python function `scipy.ndimage.label()` has been used to identify and connect regions within the binary mask. This function consists in scanning the binary image and assign a unique label to each contiguous connected region of non-zero pixels. Once these regions are identified, they can be further analyzed to extract important geometric properties e.g. size, length, width.

We approximated the PVS regions using an ellipsoid model as depicted in Figure 4.10b. By analyzing the geometric properties of the hypothetical ellipsoids, it was possible to precisely define the dimensions of the components, distinguishing the PVS from the surrounding noise in the scan and classifying the PVS based on their appearance. The use of ellipsoids proved to be particularly effective as it provides a simple yet accurate way to describe the three-dimensional shape of the PVS. The geometric properties include the size, length and width of each component. Specifically, as represented in Figure 4.10a:

1. *Size* refers to the total volume of the PVS component, which is determined by the number of voxels (3D pixels) that constitute the labeled region. This volume represents the overall extent of the PVS is space and is useful for quantifying its size.

2. *Length* is defined as the longest dimensions of the PVS and corresponds to the principal axis of the approximated ellipsoid, also known as the main elongation axis in 3D space.

3. *Width* is considered the second-longest dimension of the PVS, which can be interpreted as the second-largest axis of the approximate ellipsoid.

To compute these geometric properties, the library `skimage.measure.regionprops` has been employed.

(a) Geometric approximation of the PVS to an ellipsoid. Schematic illustration of individual PVS metrics analyzed to distinguish PVS from other brain microstructures (Ballerini et al., 2020).

(b) Representation of geometrical properties in a detected PVS. The approximate ellipsoid is in gray, the length in red and the relative width in green.

Figure 4.10: Illustration of the geometric approximation and properties of PVS.

Based on the literature (Ballerini et al., 2018), several constraint on these properties have been adapt in order to identify elongated structures (potential PVS) and isolate more likely candidates. More in details:

- **Region size filtering**: We imposed a volume range of existing for PVS regions, calculated as the approximate volume of a cylinder of radius 2.5 and length 50 voxels as a factor differentiating PVS and white matter hyperintensities (WMH). We excluded areas greater than 1000 voxels.

- **Shape constraints:** We considered those areas in which the following conditions were met:
    - The minor axis w (width) must be smaller than the major axis l (length):
    $$w < l$$
    - The minor axis must be at least 1 voxel:
    $$w \geq 1$$
    - The major axis must be between 3 and 50 voxels:
    $$3 \leq l \leq 50$$

Figure 4.12 represents a 3D rendering of the final vesselness map obtained by applying the Frangi filter and the post-processing step to the ROI (i.e. WM). In Figure 4.11 the same example is shown in axial view, comparing the vesselness map directly generated by the filter and the final vesselness map after processing.

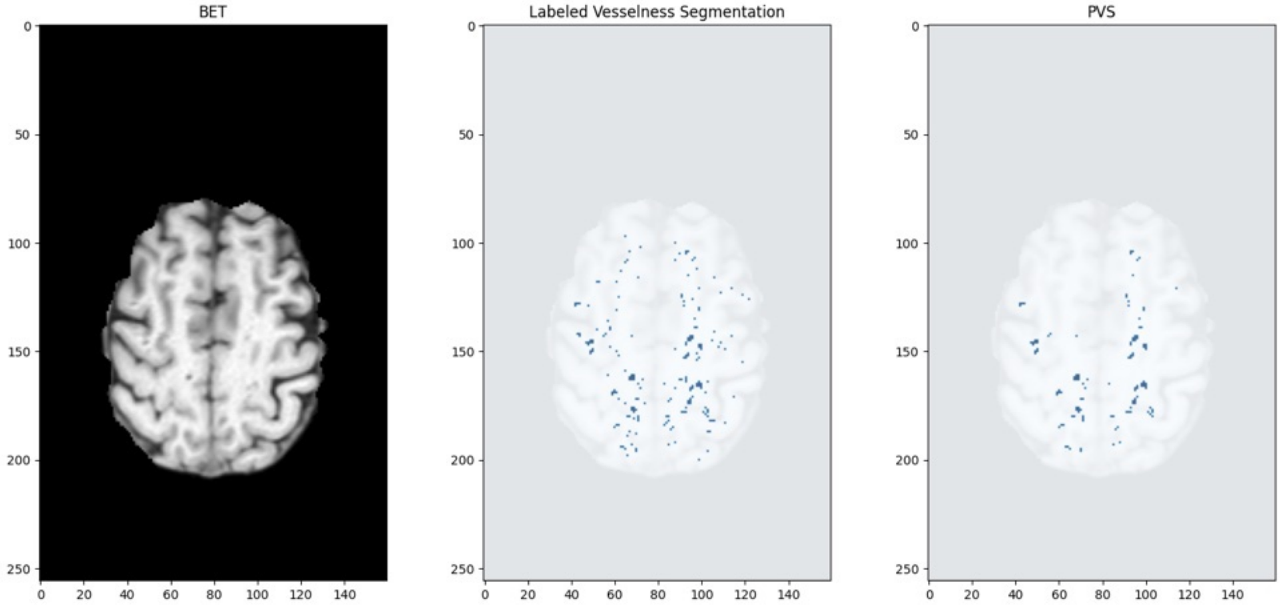

Figure 4.11: Constraints application for refined PVS isolation.

4.3 Deep-learning approach: 3D U-Net

A 3D U-Net architecture has been designed and implemented. A crucial aspect of this approach is the choice of ground truth labeling. Due to the time consuming and subjective-related in manually annotating our dataset, we adopted the PVS binary masks of the previous classical segmentation methods as the reference standard. This ensures an objective training process and a high degree of reliability in the segmentation results.

4.3.1 Neural architecture

The proposed network 4.13 is based on the classic 3D U-Net architecture, proposed by Ronneberger et al. (2015) in 2015. Structurally, it follows the characteristic "U" shape and consists of two main phases: a down-sampling phase, where the spatial information of the input features is progressively compressed to extract high-level representations and an up-sampling phase, in which the feature maps are reconstructed back to the initial spatial space.

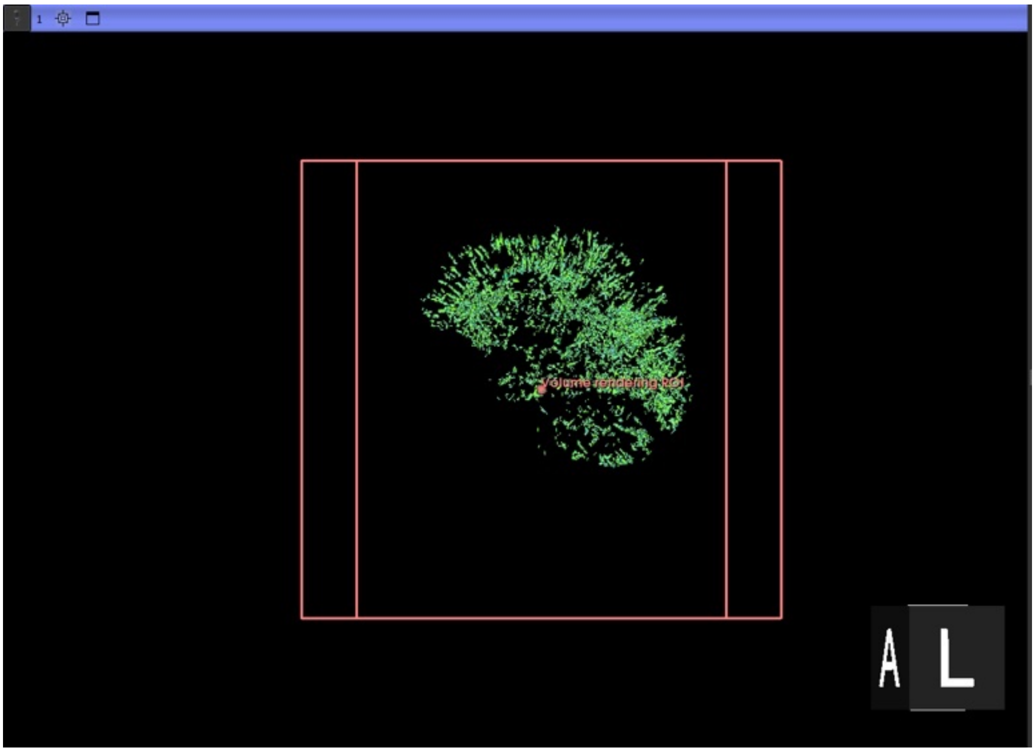

Figure 4.12: 3D rendering of PVS detection within the WM through semi-automated approach.

The network input is an MRI scan with dimensions:

$$(160, 256, 256, 1)$$

where:

- 160 represents the depth (number of slices).
- 256 × 256 represents the spatial resolution of each slice.
- 1 denotes the single-channel image (grayscale).

The down-sampling step occurs in the contracting path (encoder), stadiums where high-level features are extracted. It actually reduces the spatial size and involves five layers:

1. **Two Conv3D** layers (3D Convolutional) with Rectified Linear Unit (ReLU) activation function, for introducing non-linearity and allowing the network to learn more complex patterns and a Batch Normalization (BN) layer, helping in accelerating the training by normalizing the output of each layer and, thus, reducing the internal covariate shift (Ioffe and Szegedy, 2015).
2. **Single AvgPool3D** layer (3D Average Pooling) with a pool size of $2 \times 2 \times 2$, meaning each step reduces the spatial resolution by half along each dimension (height, width and depth).
3. **Two Conv3D** layers with a ReLU activation function and a BN layer.
4. **Single AvgPool3D** layer analogous to the second step with the addition of a 3D Spatial Dropout (SpatialDrop3D) layer with a dropout rate of 0.5.
5. **Two Conv3D** layers analogous to the third step with the addition of a 3D Spatial Dropout (SpatialDrop3D) layer with a dropout rate of 0.5. The SpatialDrop3D layer was introduced into the architecture to improve the generalization performance, which would be low due to the small training size. To precise, this layer drops entire 3D feature maps instead of randomly removing individual values with the maps. Dropping whole feature maps helps the model learn to rely less on specific features, moke the model more robust and avoid overfitting.

The filter sizes in the Conv3D layers gradually increase in size as you go deeper into the network: 8, 16, 32, 64 and 128. Schematically, the encoding layers are structured as follows:

Block 1:	8 filters
Block 2:	16 filters
Block 3:	32 filters
Block 4:	64 filters + SpatialDropout3D
Block 5:	128 filters + SpatialDropout3D

The output of the contracting path is a set of feature maps with a depth of 128 filter, representing complex and detailed information about the input data. The up-sampling step, instead, occurs in the expanding path (decoder), which is responsible for expanding the lower-dimensional features coming from contracting path and reconstructing them back to original input size. It consists in five stadiums as well with the difference that in the first four layers, a 3D Transposed Convolution (TransposeConv3D) layer was used instead of the 3D up-sampling layer, followed by one Conv3D layer with ReLU activation function. The operation is called "deconvolution" since it reverses the effect of a regular convolution. This layer is followed by a Concatenation (Concat) layer for skipping connection and two Conv3D layers with ReLU activation function and a BN layer. Concatenating the up-sample feature maps with the corresponding feature maps from the encoder (skip connections) we can retrain information lost during down-sampling. Schematically, the decoding layers are structured as follows:

Block 6:	64 filters
Block 7:	32 filters
Block 8:	16 filters
Block 9:	8 filters

Finally, last layer consists of a Conv3D layer with Sigmoid activation function for refining the up-sampled feature maps. Since this is a binary segmentation task, we applied a 3D convolution with kernel size $1 \times 1 \times 1$.

$$\text{Conv3D}(1, 1, \text{activation} = \text{sigmoid})$$

where:

- 1 represents the class probability of PVS.
- $\sigma(x) = \frac{1}{1+e^{-x}}$ is the sigmoid activation function, ensuring the output is between 0 and 1.

The final output of this layer is a 3D probability map of the same spatial size as the input MRI where each voxel has a probability between 0 and 1 of belonging to the PVS class. Values close to 1 mean high confidence that the voxel belongs to PVS class, values close to 0 mean high confidence they not belong to it. Hence, through a following thresholding step we can generate a binary segmentation mask of PVS automatically.

Data preparation

Dataset The dataset consists of MRI scans representing only the brain tissues and their corresponding ground truth labels. The labels coming from semi-automatic annotation applied Frangi filter and a sequent manual correction of a neuroradiologist. The dataset includes MRI scans from subjects diagnosed with PD.

Data augmentation Due to the small size and low presence of PVS the dataset is very sparse. To enable more robust learning of the model from the data, control and reduce overfitting, data augmentation was applied. The augmentation was applied only to the training set so that neither the validation nor the test set could cause bias. Given the intrinsic symmetry of the brain, we chose to apply horizontal flip augmentation.

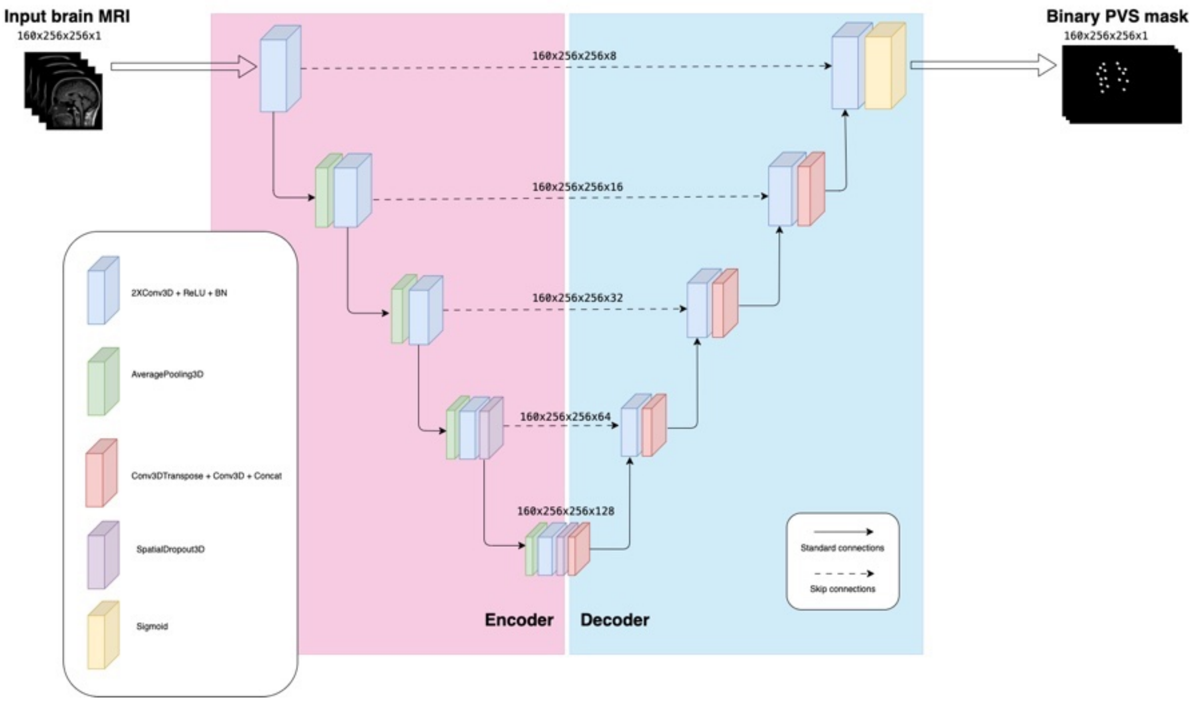

Figure 4.13: 3D U-Net architecture.

Data division The data split was performed at subject-level, being careful not to include data belonging to the same subject within the training, validation and test sets. The MRI images were divided as follow:

- Training set: 90% of the entire dataset, corresponding to 148 MR volumes and 74 subjects
- Validation set: 5% of the entire dataset, corresponding to 10 MR volumes and 5 subjects
- Test set: 5% of the entire dataset, corresponding to 10 MR volumes and 5 subjects

To clarify, each subject is represented by two scans: one taken at time T0 and another at the follow-up time T1. Therefore, when working with data coming from a single subject, it involves handling two scans captured at different time points.

Learning process

The 3D model was implemented in Python using the Keras APIs of TensorFlow. Keras APIs are based on two main type of data structures: layers and models. A model is a directed acyclic graph (DAG) of layers, where each layer represents a simple transformation with an input and an output.

The fundamental class in Keras is tf.keras.layers.Layer, which encapsulates both weights and computational operations. A model, on the other hand, is an object that groups multiple layers and can be trained on a dataset. Keras provides directly in the tf.keras.Model class methods for the training and evaluation phase of the model. In particular, the methods adopted are:

- compile(): method with which the model can be built. The metrics (Accuracy, Dice Coefficient, IoU, etc.), the loss function (Binary Cross Entropy, Dice Loss, Focal Loss) and the optimizer (e.g. SGD, Adam, Adagrad, RMSprop) must be specifically selected to proceed and adapt the learning process to the task.
- fit(): method to train the model with a fixed number of epochs. Advanced features, such as callbacks, can be defined so that the model can be monitored, saved, or stopped early.
- predict(): method by which the model generates predictions based on the learning process
- estimate(): method to evaluate the learning process. Returns the final value of the loss function and the final values of the metrics specified in the compile method

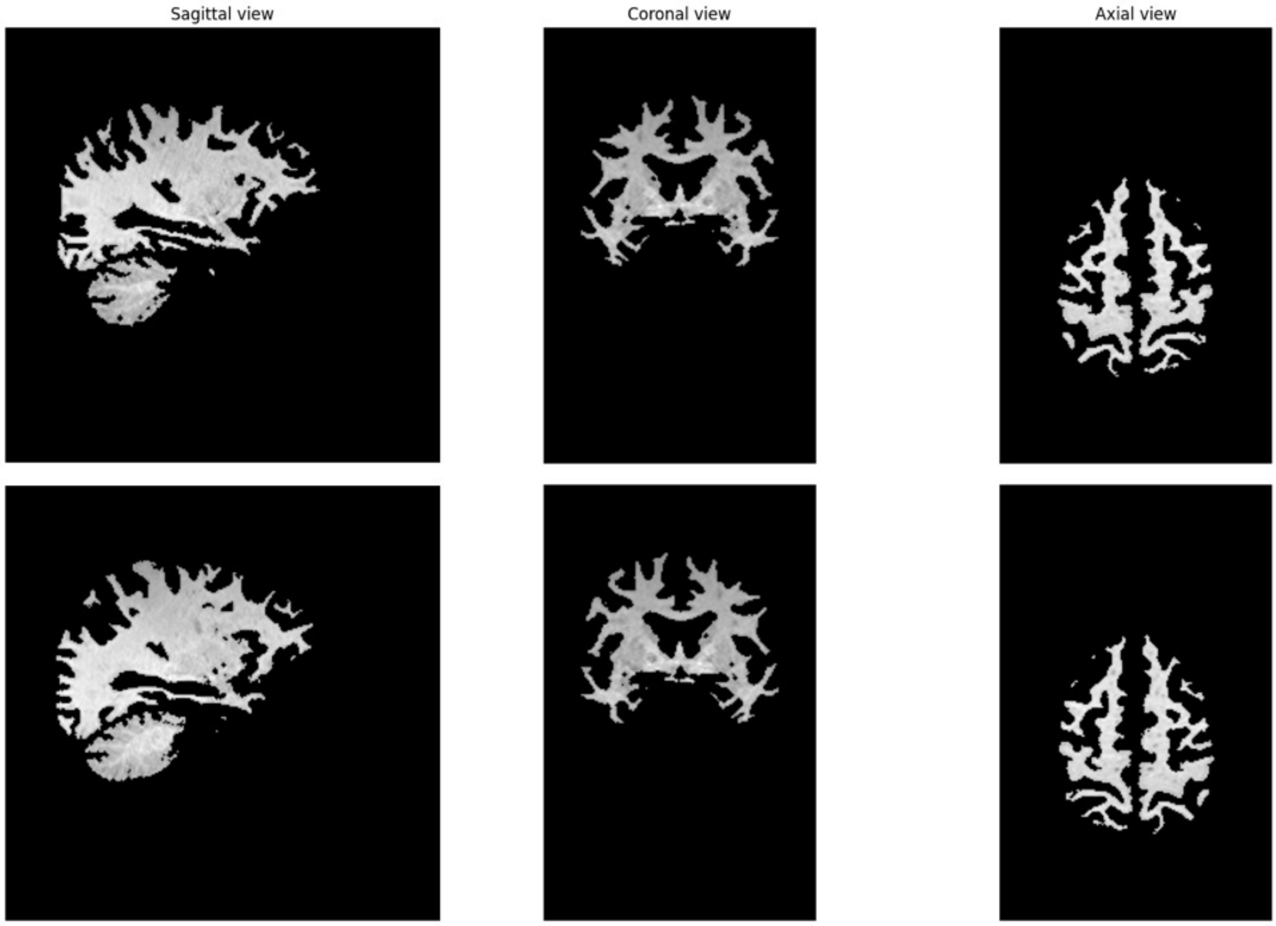

Figure 4.14: Horizontal flipping augmentation technique.

Loss function and optimization The implemented 3D model was trained from scratch for 50 epochs, using a batch size of 1 and a learning rate of 0.01. The RMSprop optimizer was chosen. Callbacks for early stopping, model checkpoints and plateau learning rate reduction were adopted to reduce overfitting. Overall, we proposed a model that aimed to maximize segmentation performance while mitigating the challenges posed by class imbalance.

To overcome the sparse and unbalanced dataset problem, we used a combined loss composed of weighted Dice loss (WDL) and focal Loss (FL) as the loss function. PVS, in fact, are very small structures compared to the whole brain and cause a strong class imbalance between the background and target regions, hindering the learning process.

The FL function is particularly effective in addressing class imbalance during training on tasks such as object detection (Lin et al., 2017). In practice, FL adds a factor to the standard cross-entropy loss such that learning focuses more on difficult examples, giving less importance to more representative classes.

$$\mathscr{L}_{\mathrm{FL}} = -\alpha_t (1 - p_t)^{\gamma} \log(p_t)$$

where:

- p_t is the predicted probability of the correct class.
- α_t is an assigned weight to balance classes. In our case $\alpha_t = 0.5$.
- γ (gamma factor) controls the model focus on difficult samples. In our case $\gamma = 2$.

An effective loss function for segmentation in medical images is the Dice loss. It derives from the Dice similarity coefficient (DSC), coefficient used for measuring the overlap between the prediction and the label segmentation. Mathematically,

$$\mathcal{L}_{\text{dice}} = 1 - \frac{2\sum y_{\text{true}} y_{\text{pred}} + \epsilon}{\sum y_{\text{true}} + \sum y_{\text{pred}} + \epsilon}$$

where:

- y_{true} is the real mask.
- y_{pred} is the predicted mask.
- ϵ is a small value to avoid dividing by zero.

The issue when dealing with target structures really small with respect to the background, as in our case the PVS are, is that the loss could not be enough for correctly adjusting the learning not penalizing enough the error regions. We addressed this problem by introducing a different weight for the background and the target structures, increasing the contribution of smaller structures. Basically, the WDL can be written as follow:

$$\mathcal{L}_{\text{WDL}} = 1 - \frac{2\sum w_i y_{\text{true}} y_{\text{pred}} + \epsilon}{\sum w_i y_{\text{true}} + \sum w_i y_{\text{pred}} + \epsilon}$$

where w_i is the weight of the voxel i based on its classification. A voxel classified as PVS will weight more than a voxel classified as background. In this way we were able to tackle the unbalanced data problem.

The final loss function is :

$$\mathcal{L} = \lambda_1 \mathcal{L}_{\text{WDL}} + \lambda_2 \mathcal{L}_{\text{FL}}$$

where λ_1 e λ_2 are hyperparameters for balance the two losses.

RMSprop was used as the optimizer. The algorithm is a variant of the gradient descent algorithm. While SGD uses constant learning rates and AdaGrad reduces the learning rate too aggressively, RMSProp improves the performance and training speed of DL models by adapting the learning rates based on a moving average of squared gradients. These features make the optimizer efficient in training DL models, especially when dealing with noisy data or with gradients that can vary significantly between different tensor sizes.

Performance evaluation The model has been evaluated on test data, considering the best checkpoint obtained during the training process. We save the models with lowest validation loss and the weights of the higher dice coefficient obtained.

The evaluation of the performance was based on the comparison between the labels and the predictions. The main metric used for the evaluation was DSC.

4.3.2 Segmentation of perivascular spaces

Count and volume measure analysis The number of PVS and the total volume were computed.

The number was easily computed by counting the recognized connected components. For computing the total volume across all detected connected components, we calculated the volume of singular component and sum them up together. The volume is expressed in mm^3.

$$V_{\text{total}} = \sum_{i=1}^{N} V_i = \sum_{i=1}^{N} |C_i| \cdot V_v$$

Since each voxel has a unitary volume ($V_v = 1\,\text{mm}^3$), the total volume simplifies to:

$$V_{\text{total}} = \sum_{i=1}^{N} |C_i|.$$

where:

- N is the total number of detected PVS.
- $|C_i|$ is the cardinality of the connected component C, i.e. number of voxels belonging to the connected component C.

- V_v is the volume of each voxel. Based on the given dataset acquisition techniques, this value is 1 mm^3, reducing the volume computation to the count of PVS-classified voxels.

4.4 Volumetric rendering

In order to visualize the small fluid-structures in details and represent as much as possible the complex glymphatic sistem, we rendered the resulting vesselness maps in 3D. Several software are available for 3D rendering of medical images such as InVesalius and 3D Slicer. In this research, both software have been exploited for the visualization of the data but Slice3D was preferred over the other tool, mainly because of its intuitive user-interface and amount of advanced features such as the possibility of visualizing more than one single MRI scan at the same time.

In the contest of PVS visualization, the use of techniques of 3D rendering (Figure 4.15) allows to obtain highly realistic representations, useful in the understanding the anatomical structure of the glymphatic system and, indirectly, comprehend complex physiological phenomena such as the response to glymphatic system damage, crucial for clinical research and treatment of several associated brain conditions.

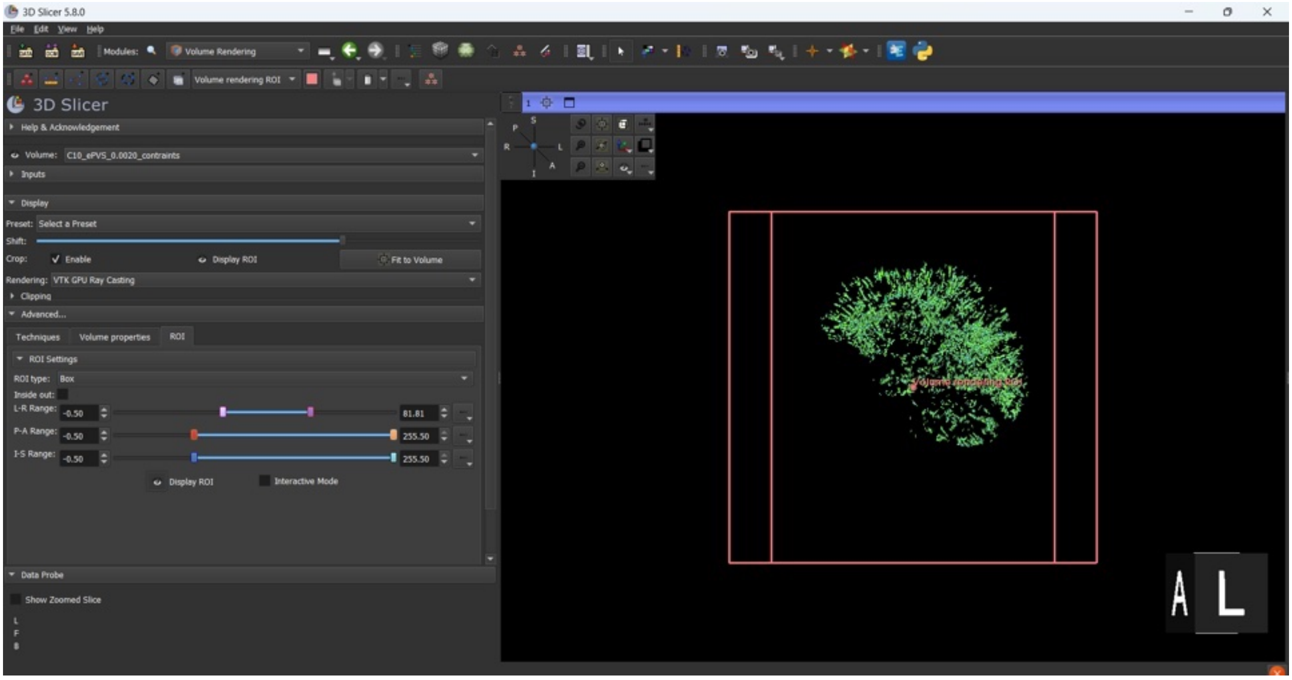

Modules: Volume Rendering

Volume: C10_ePVS_0.0020_contraints

Preset: Select a Preset

Crop: ✓ Enable

Rendering: VTK GPU Ray Casting

ROI type: Box

Inside out: ☐

L-R Range: -0.50 81.81

P-A Range: -0.50 255.50

I-S Range: -0.50 255.50

☐ Interactive Mode

☐ Show Zoomed Slice

Figure 4.15: Graphical UI of the volume rendering module in Slicer3D

Chapter 5

Experimental results

This chapter gives a qualitative and quantitative evaluation of the approaches previously described in PVS segmentation. We assessed the performance of both the semi-automated and fully-automated methods through extensive statistical and longitudinal analyses.

5.1 Segmentation task

The semi-automated method consisted in the combination of Frangi filter-based vesselness map and manual corrections. The fully-automated method, instead, consisted in a 3D U-Net model trained on pre-processed brain MRI data to segment the PVS regions automatically.

5.1.1 Qualitative analysis: semi-automated approach vs automated approach

The semi-automated approach was qualitatively analyzed in the initial stages of this project during the definition of the constraints, in particular when different vesselness thresholds were studied to include hypothetical PVS and exclude irrelevant tubular structures. The final vesselness threshold selection was based on statistical analysis. In Table 5.1 we report the p-values of the analysis performed to evaluate the correlation between the PVS volume and relevant clinical variables, all resulted to be continuous. Depending on the single variable, we computed the correlations either at T0, T1 or both at T0 and T1 (the reason why some data entry are empty). For instance, the sleep values were statistically compared with PVS volume at T1 as they describe sleep patterns (media and average) during the study period of one month. The values marked with a star sign indicate those entries whose p_value is below the statistical level of significance, thus deemed as clinically relevant.

Threshold	**Time**	**UPDRS I**	**UPDRS II**	**UPDRS III**	**SLEEP (avg)**	**SLEEP (median)**	**LEDD**
0.002	T0	0.0891	0.2391	0.0273*	-	-	0.44948
0.002	T1	0.5084	0.8503	0.5277	0.0308*	0.0078*	0.2567
0.0002	T0	0.0642	0.4350	0.7306	-	-	0.9684
0.0002	T1	0.2846	0.7196	0.8962	0.6728	0.8420	0.3738

Table 5.1: Statistical analysis between each clinical variable v and the total PVS volume at each threshold t.

Considering the threshold 0.002, we observe three clinical correlations. Interestingly, the first correlation is related to UPDRS III with a Spearman value of -0.3220, indicating a moderate negative correlation. Thus, the volume of PVS and the UPDRS III value are inversely proportional. The second clinical correlation arises from the sleep variable, from both median and average values. Both values correlate positively, namely that they are directly proportional. At threshold 0.0002, instead, no statistical significance were observed, indicating that this threshold does not hold clinical correlation.

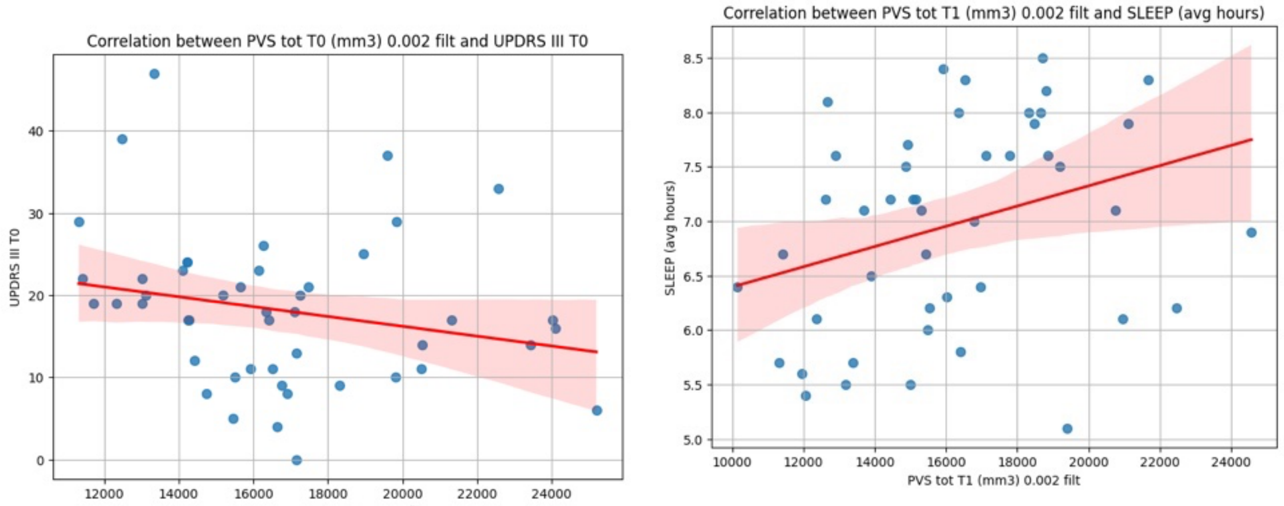

(a) Correlation between total PVS volume at T0 (in mm³) and UPDRS III score at T0. The regression line indicates a negative trend, suggesting a possible inverse association between these parameters.

(b) Correlation between total PVS volume at T1 (in mm³) and mean sleep duration (in hours) up to the day before T1 control. The regression line shows a positive relationship, suggesting that a larger PVS volume may be associated with longer sleep.

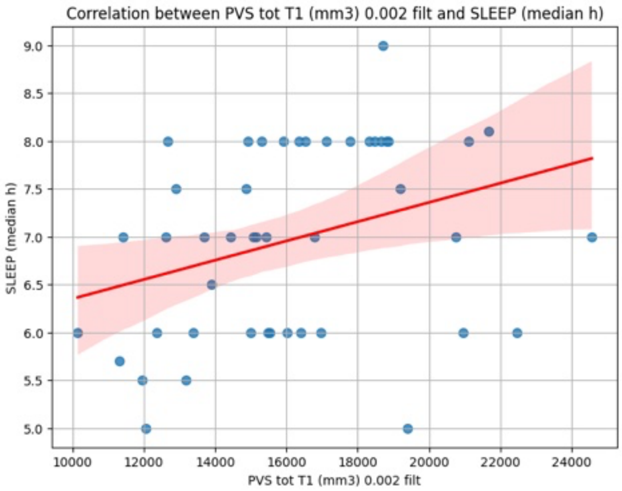

(c) Correlation between total PVS volume at T1 (in mm³) and median sleep duration (in hours) up to the day before T1 control. A positive trend is observed, indicating a possible relationship between a larger PVS volume and a longer sleep duration.

Figure 5.1: Scatter plots.

Based on these considerations, 0.002 was selected as the optimal threshold for PVS segmentation in the semi-automated approach. The neuroradiologist validated this choice, confirming its accuracy and the overall reliability of the semi-automated method in delinating PVS. In practice, the clinician visually inspected whether the semi-automated approach was able to capture the correct structures and whether there were evident errors, such as missing or false segmentation. The presence of noise and artifacts was also assessed.

Similarly for the semi-automated approach evaluation, also in the fully-automated approach the neuroradiologist had to carefully examine the outputs to determine whether the model correctly captured the target spaces without including non-relevant structures. This visual inspection was performed by looking at the original scans and at the output of the semi-automated approach, already considered clinically valid. In Figure 5.2, we can observe the PVS detected by the Frangi filter-based method (i.e. true mask) and the deep learning-based method (i.e. prediction mask). A map of PVS detected through both approaches has been created for helping the qualitative analysis.

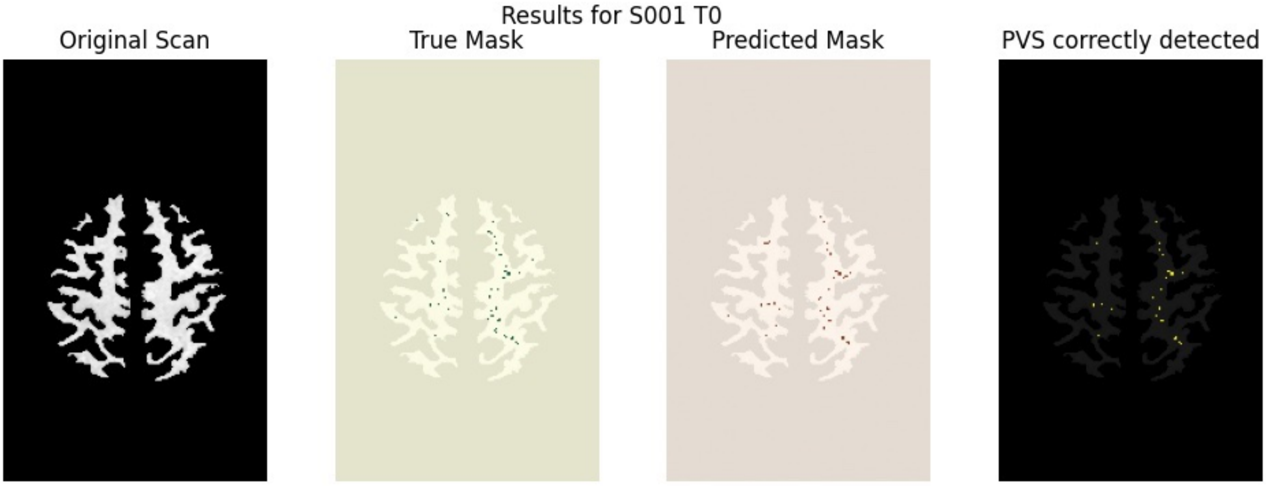

Figure 5.2: Qualitative analysis: WM extraction on the left, PVS segmentation through semi-automated and fully-automated approach in the center and PVS detected in both the approaches on the right.

It is evident that the 3D U-Net model correctly detects the structures in a good amount but there are also evident detected structures not present in the outcome of the semi-automated approach, taken as ground truth.

5.1.2 Quantitative analysis: semi-automated approach vs automated approach

Several experiments have been conducted for the automated approach, many of which resulted in overfitting. To mitigate this attitude, the model was fine-tuned by adjusting hyper parameters, balancing computational cost and segmentation performance. Specifically, we balanced the accuracy and speed of the model by fine-tuning the follow hyper parameters:

- Learning rate: adjusting the learning rate we prevented divergence and excessively slow learning. The selected factor was 0.001.
- Number of epochs: setting high number of epochs can lead to overfitting, while too few epochs may prevent the model from learning effectively. A valid number of epochs is crucial to select to ensure proper learning. In our study, the model was trained for 50 epochs.
- Batch size: the batch size was optimized to balance computational efficiency and gradient estimation stability. Given memory constraints, a batch size of 8 was selected.

Moreover, to further reduce overfitting, data augmentation was added to the pipeline. As a result, the final model did not exhibit severe overfitting, as evidenced in Figure 5.3. The learning curves indicate that the model is learning effectively, with only very mild overfitting. Both the training loss and validation loss decrease significantly at the beginning, showing proper learning and while the validation loss starts fluctuating slightly after approximately 10–15 epochs, the divergence between the two curves remains minimal. The validation loss does not increase significantly, suggesting that the model is not strongly overfitting, though minor oscillations indicate some sensitivity to the dataset. Overall, overfitting is extremely mild and does not appear to be a major concern. As evaluation metric, DSC measures the overlap between predicted and

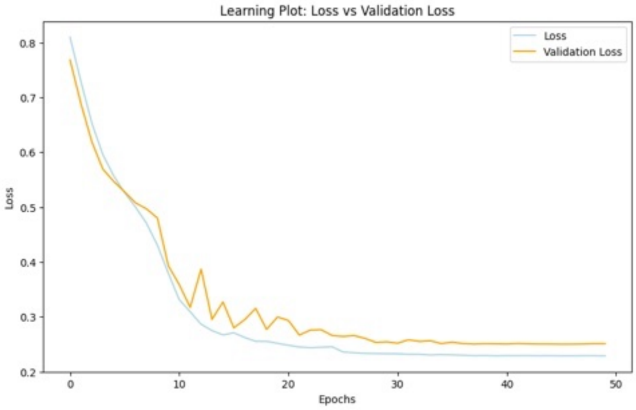

Figure 5.3: Learning plot of the implemented 3D U-Net.

ground truth segmentation. Higher values of DSC indicate high segmentation performance, while lower values of DSC indicate poor performance in detecting the target structures. It is defined as:

$$\mathrm{DSC} = \frac{2 \cdot \mathrm{TP}}{2 \cdot \mathrm{TP} + \mathrm{FP} + \mathrm{FN}}$$

In addition, volume similarity (VS) was considered as it measures the difference in the volumes between the predicted (PV) and ground truth (GT) segmentation and is defined as:

$$\mathrm{VS} = \frac{2 \cdot \mathrm{PV} \cap \mathrm{GT\ Volume}}{\mathrm{PV} + \mathrm{GT\ Volume}}$$

From a quantitative viewpoint, it seems that the fully-automated approach struggles to accurately delineate PVS, leading to suboptimal segmentation performance. In detail, the neural network reached a DSC of 0.60 and a VS of 0.80. Several factors contributed to such sub-optimal performance, primarily the poor resolution of input images. This resolution might be insufficient to accurately detect, isolate and segment very small brain structures like PVS. In particular, the down-sampling and up-sampling stages of the neural network could cause the loss of important information, negatively impacting the performance. Higher resolution images would certainly guarantee the capture of the thinnest details. The limited amount of available input data is another factor contributing to the model's sub-optimal performance. Apart from training data augmentation, this issue could not have been mitigated by publicly available data, as, to the best of our knowledge, none exist. Lastly, but not less important, the class imbalance problem. Given the complexity of brain microstructure represented in MRI input scans, the target object, PVS, occupy a very small fraction of the total brain volume, leading to a significant class imbalance and a notable bias toward background classification.

The main drawback of the model is the prediction of structures not detected in the ground truth, the so called false positives. However, being the ground truth itself strongly threshold-dependent, the quantitative analysis may not provide a fully reliable assessment of the global performance of the fully-automated approach in a clinical setting. To overcome this limitation and provide a more comprehensive evaluation of the effectiveness of the study beyond standard segmentation metrics, the neuroradiologist conducted a further visual inspection, exploring the resulting vesselness map of the neural network after applying an additional step of post-processing, i.e. the same for the semi-automated approach, based on the selection of connected components with a certain area. This process contributed in removing a lot of false positives, resulting in a more reliable vesselness map. In Figure 5.4 an example of the resulting map of PVS.
Therefore, although the model failed to achieve optimal performance in segmenting such microstructures, the neuroradiologist recognized the value of both approaches as promising tools for diagnostic support, rating the output of both models as clinically acceptable.

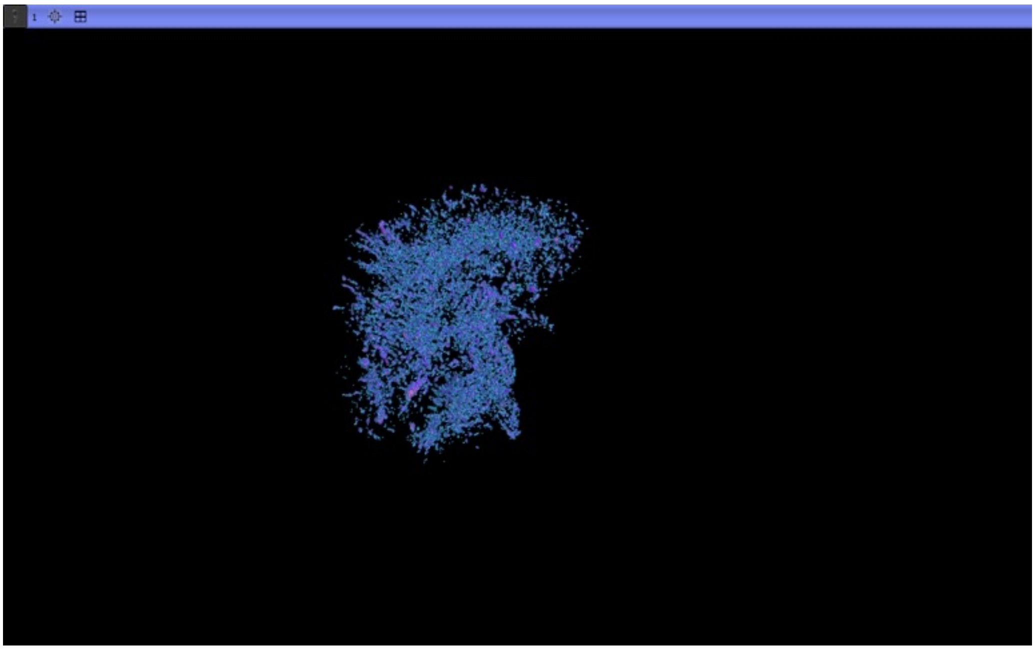

Figure 5.4: Vesselness map detected by 3D U-Net model with post-processing stage added to the pipeline.

5.2 Longitudinal study

The clinical objective was implementing a valid segmentation method for studying the changes in PVS over time. A longitudinal study, hence, has been conducted, meaning the study of repeated observations of the same variables over time. The purpose of this additional analysis is to discuss the changes in PVS volume after one month (i.e. Is there a significant increase or decrease in PVS volume over time?). The analysis has been performed on five patients, each with two associated scans, one at time T0 and the other at time T1, one month later. For both time points, PVS count were computed as the total number of the connected components for the whole volume. Such analysis was performed using a single methodology, based on the results of the approach considered the clinical gold standard: the semi-automated one.

Subject	PVS TV (mm^3) T0	PVS TV (mm^3) T1	PVS TV (mm^3) T1 - T0
S001	13331	12609	-722
S002	16336	15087	-1249
S003	23419	19399	-4020
S004	16903	13388	-3515
S005	15176	13188	-1988

Table 5.2: Comparison of PVS total volume (TV) at different time points.

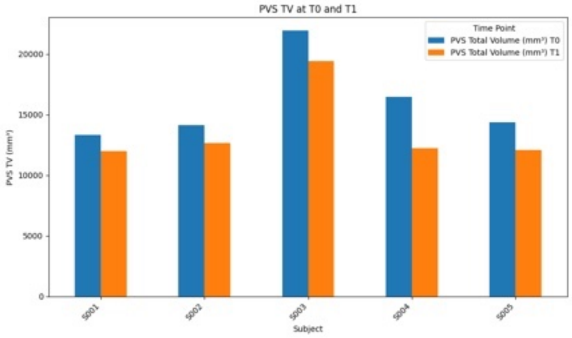

Figure 5.5: Graphical representation of PVS total volume in subsequent phases T0 and T1 among a restricted yet significant cohort of subjects.

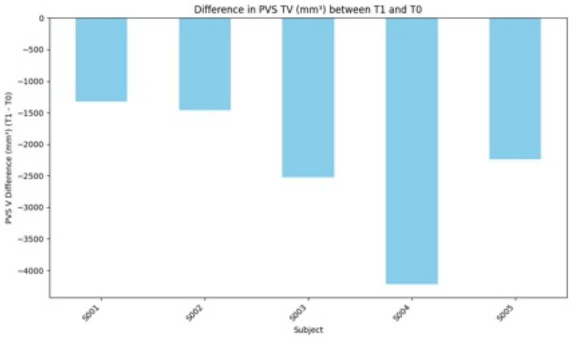

Figure 5.6: Graphical representation of PVS total volume difference between time point T0 and T1 among a restricted yet significant cohort of subjects.

From the graphical representation in Figure 5.6 we can observe a common trend of volume decrease. This result is impressive as it suggests a measurable reduction in PVS over time, potentially indicating an improvement in glymphatic system as a response to the applied treatment. Since the decrement on glymphatic functions and the PVS have been associated with different neurodegenerative conditions, including PD and its decline, a reduction in their number and volume could reflect in beneficial changes in the brain. From a clinical perspective, this finding may support the hypothesis that targeted treatments, such as cognitive and motor exercises, can positively influence brain microstructure indirectly affecting on the disease. Future studies could further validate these results by analyzing a larger cohort and investigating the underlying physiological mechanisms contributing to PVS enlargement.

Chapter 6

Conclusions

This chapter sums up the content of this thesis, focusing on the theoretical and practical results produced by our study on PVS and my personal contribution to this ambitious project.

The project idea is coming from an intuitive observation of a neuroradiologist expert in analyzing MRI scans for evaluating patients' tissues and organs conditions. The doctor demanded the implementation of a pioneering yet valid method for delineating PVS in MRI scans of a cohort of PD patients, visually observing changes in their cardinality and volume when time progressed. The project, hence, focused on the automatic segmentation and both quantitative and qualitative analysis of PVS, implementing a deep learning-based approach and a semi-automatic method converging in the Frangi filter employment. According to the aim of this thesis, we experimented the effectiveness of such methodologies and investigated potential changes in PVS volume over time.

For these purposes, the processing pipeline is composed of multiple interconnected stages disegned to ensure a comprehensive analysis of perivascular spaces. It begins with an image pre-processing phase with the aim of preparing the data for later analysis. It consisted in enhancing image quality and reducing as much as possible the noise, collected in the acquisition process. Following this phase, two distinct segmentation approaches are implemented: one semi-automatic and the other automatic. In particular, the semi-automatic approach relies on traditional image processing techniques such as filtering and thresholding while the automatic approach is based on deep learning, specifically a 3D U-Net. Once segmentation is completed, a post-processing phase is applied with the aim of refining the detected structures, improving accuracy and consistency of the results. The segmented maps, then, undergoes qualitative, quantitative, statistical and analyses to extract meaningful insights in PVS evolution. Lastly, to visualize and facilitate interpratation of PVS structures and glymphatic system, the extracted PVS volumes are rendered in three-dimensional space using the volume rendering module of Slicer3D framework.

In the statistical analysis, different statistical tests are conducted to assess the clinical correlations between PVS volume and continuous variables such as sleep duration, LEDD and other relevant clinical factors. We observed valid correlations with the UPDRS III value and hours of sleep, in a positive and negative way, respectively. Regarding the longitudinal analysis, 100% of the tested subjects showed a reduction in PVS number and volume at time T1 compared to time T0, a relevant prognostic factor. In particular, the longitudinal analysis confirmed the intuition and hypothesis raised by the clinician. We observed a general trend of decreasing volume over time of the segmented PVS. This observation suggests potentially beneficial effects of the proposed therapy in PD and could provide insights into disease progression. More generally, a valid longitudinal study could explain the impact of specific treatments in Parkinson's.

While the current project provides valuable insights, several improvements can be made in future research, where we want to address the weaknesses in order to foster reproducibility and encourage new solutions. First, data were acquired with a lower magnetic field (i.e., 1.5 Tesla) than those indicated in the literature, where at least 3 Tesla is suggested. It is likely that by improving the resolution, the neural network's performance would increase. The dataset cardinality was also scarce. Our dataset consists of 47 subjects, each associated with two MRI scans taken at different time points, T0 and T1, one month apart. It is evident that this number is insufficient to populate a robust dataset capable of adequately training and testing a deep learning architecture. At the very least, this represents a bottleneck for the neural network's generalization capabilities, given the limited number of samples available for learning. This challenge was partially mitigated using training data augmentation, which unfortunately did not yield sufficient results to fully resolve the issue. Additionally, the semi-automated approach used to generate labels for segmenting PVS, which served as the ground truth, introduced an extra step in the pipeline, further slowing the workflow and introducing a certain degree of cognitive bias. Another critical aspect is that PVS are extremely small structures, making them prone to misclassification when morphological constraints or size-based criteria are not applied. Without such constraints, segmentation relies primarily on pixel intensity (gray-level values), which may lead to confusion with other similar structures, further challenging the model's accuracy.

Since the project does not stop here, we now discuss the future steps of the research. The main future step is to refine the deep learning model as well as test other architectures, such as vision transformers. We also want to suggest to increase the sample quantity, for both model learning and longitudinal analysis purposes. By making more subjects join the study, the results would benefit from an increased statistical relevance and the neural network would surely better generalize, having more samples to learn from. In addition, considering some other brain regions like BG, besides only the WM region, could represent a significant step forward in PVS interpretation. Eventually, the combination of multi-modal imaging techniques, such as T1-weighted, T2-weighted and FLAIR sequences, could help in distinguishing PVS regions from similar microstructures by leveraging on the distinct characteristics of these modalities.

Bibliography

B. B. Avants, N. J. Tustison, G. Song, P. A. Cook, A. Klein, and J. C. Gee. A reproducible evaluation of ants similarity metric performance in brain image registration. *Neuroimage*, 54(3):2033–2044, 2011.

L. Ballerini, R. Lovreglio, M. D. C. Valdés Hernández, J. Ramirez, B. J. MacIntosh, S. E. Black, and J. M. Wardlaw. Perivascular spaces segmentation in brain MRI using optimal 3D filtering. *Sci. Rep.*, 8(1):2132, Feb. 2018.

L. Ballerini, S. McGrory, M. d. C. V. Hernández, R. Lovreglio, E. Pellegrini, T. MacGillivray, S. M. Maniega, R. Henderson, A. Taylor, M. E. Bastin, et al. Quantitative measurements of enlarged perivascular spaces in the brain are associated with retinal microvascular parameters in older community-dwelling subjects. *Cerebral Circulation-Cognition and Behavior*, 1:100002, 2020.

G. Barisano, N. Sheikh-Bahaei, M. Law, A. W. Toga, and F. Sepehrband. Body mass index, time of day and genetics affect perivascular spaces in the white matter. *J. Cereb. Blood Flow Metab.*, 41(7):1563–1578, July 2021.

J. Bernal, M. D. Valdés-Hernández, J. Escudero, R. Duarte, L. Ballerini, M. E. Bastin, I. J. Deary, M. J. Thrippleton, R. M. Touyz, and J. M. Wardlaw. Assessment of perivascular space filtering methods using a three-dimensional computational model. *Magnetic Resonance Imaging*, 93:33–51, 2022.

S. Bhat, U. R. Acharya, Y. Hagiwara, N. Dadmehr, and H. Adeli. Parkinson's disease: Cause factors, measurable indicators, and early diagnosis. *Comput. Biol. Med.*, 102:234–241, Nov. 2018.

E. L. Boespflug, D. L. Schwartz, D. Lahna, J. Pollock, J. J. Iliff, J. A. Kaye, W. Rooney, and L. C. Silbert. MR imaging-based multimodal autoidentification of perivascular spaces (mMAPS): Automated morphologic segmentation of enlarged perivascular spaces at clinical field strength. *Radiology*, 286(2):632–642, Feb. 2018.

P. Boutinaud, A. Tsuchida, A. Laurent, F. Adonias, Z. Hanifehlou, V. Nozais, V. Verrecchia, L. Lampe, J. Zhang, Y.-C. Zhu, C. Tzourio, B. Mazoyer, and M. Joliot. 3d segmentation of perivascular spaces on t1-weighted 3 tesla mr images with a convolutional autoencoder and a u-shaped neural network. *Frontiers in Neuroinformatics*, 15, 2021. doi: 10.3389/fninf.2021.641600. URL `https://www.scopus.com/inward/record.uri?eid=2-s2.0-85110188306&doi=10.3389%2ffninf.2021.641600&partnerID=40&md5=cad58090b737c189607bd7d602bea05b`. cited By 23.

D. Cai, M. Pan, C. Liu, W. He, X. Ge, J. Lin, R. Li, M. Liu, and J. Xia. Deep-learning-based segmentation of perivascular spaces on t2-weighted 3t magnetic resonance images. *Frontiers in Aging Neuroscience*, 16, 2024. doi: 10.3389/fnagi.2024.1457405. URL `https://www.scopus.com/inward/record.uri?eid=2-s2.0-85203804017&doi=10.3389%2ffnagi.2024.1457405&partnerID=40&md5=951c1c0737dc9c1afc702ccd73051342`. cited By 0.

S. T. Chan, N. D. Mercaldo, B. Ravina, S. M. Hersch, and H. D. Rosas. Association of dilated perivascular spaces and disease severity in patients with huntington disease. *Neurology*, 96(6):e890–e894, 2021.

Y. Choi, Y. Nam, Y. Choi, J. Kim, J. Jang, K. J. Ahn, B.-S. Kim, and N.-Y. Shin. MRI-visible dilated perivascular spaces in healthy young adults: A twin heritability study. *Hum. Brain Mapp.*, 41(18):5313–5324, Dec. 2020.

E. K. Donahue, A. Murdos, M. W. Jakowec, N. Sheikh-Bahaei, A. W. Toga, G. M. Petzinger, and F. Sepehrband. Global and regional changes in perivascular space in idiopathic and familial parkinson's disease. *Mov. Disord.*, 36(5):1126–1136, May 2021.

E. K. Donahue, R. P. Foreman, J. J. Duran, M. W. Jakowec, J. O'Neill, A. J. Petkus, D. P. Holschneider, J. Choupan, J. D. Van Horn, S. Venkadesh, et al. Increased perivascular space volume in white matter and basal ganglia is associated with cognition in parkinson's disease. *Brain Imaging and Behavior*, 18(1): 57–65, 2024.

F. Dubost, H. Adams, G. Bortsova, M. Ikram, W. Niessen, M. Vernooij, and M. de Bruijne. 3d regression neural network for the quantification of enlarged perivascular spaces in brain mri. *Medical Image Analysis*, 51:89–100, 2019a. doi: 10.1016/j.media.2018.10.008. URL `https://www.scopus.com/inward/record.uri?eid=2-s2.0-85055753914&doi=10.1016%2fj.media.2018.10.008&partnerID=40&md5=c5fd4d81e2f1b94f6873d1e2367a2f6a`. cited By 42.

F. Dubost, P. Yilmaz, H. Adams, G. Bortsova, M. Ikram, W. Niessen, M. Vernooij, and M. de Bruijne. Enlarged perivascular spaces in brain mri: Automated quantification in four regions. *NeuroImage*, 185:534–544, 2019b. doi: 10.1016/j.neuroimage.2018.10.026. URL `https://www.scopus.com/inward/record.uri?eid=2-s2.0-85055525908&doi=10.1016%2fj.neuroimage.2018.10.026&partnerID=40&md5=5c72946c5537b7b0e3ecdacd2f96b173`. cited By 77.

Y. Fang, L.-Y. Gu, J. Tian, S.-B. Dai, Y. Chen, R. Zheng, X.-L. Si, C.-Y. Jin, Z. Song, Y.-P. Yan, X.-Z. Yin, J.-L. Pu, and B.-R. Zhang. MRI-visible perivascular spaces are associated with cerebrospinal fluid biomarkers in parkinson's disease. *Aging (Albany NY)*, 12(24):25805–25818, Nov. 2020.

B. Fischl. Freesurfer. *Neuroimage*, 62(2):774–781, 2012.

A. Frangi, W. Niessen, K. Vincken, and M. Viergever. Multiscale vessel enhancement filtering. In W. Wells, A. Colchester, and S. Delp, editors, *Medical Image Computing and Computer-Assisted Intervention - MICCAI 1998 - 1st International Conference, Proceedings*, Lecture Notes in Computer Science (including subseries Lecture Notes in Artificial Intelligence and Lecture Notes in Bioinformatics), pages 130–137, Italy, 1998. Springer-Verlag Italia. ISBN 3540651365. doi: 10.1007/bfb0056195. Publisher Copyright: © Springer-Verlag Berlin Heidelberg 1998.; 1st International Conference on Medical Image Computing and Computer-Assisted Intervention, MICCAI 1998 ; Conference date: 11-10-1998 Through 13-10-1998.

K. Gouveia-Freitas and A. J. Bastos-Leite. Perivascular spaces and brain waste clearance systems: relevance for neurodegenerative and cerebrovascular pathology. *Neuroradiology*, 63(10):1581–1597, Oct. 2021.

Q. Gui, J. Meng, M. Shen, H. Feng, X. Dong, D. Xu, W. Zhu, Q. Cheng, L. Wang, G. Wu, and Y. Lu. Relationship of glymphatic function with cognitive impairment, sleep disorders, anxiety and depression in patients with parkinson's disease. *Neuropsychiatr. Dis. Treat.*, 20:1809–1821, Sept. 2024.

P. Huang, L. Liu, Y. Zhang, S. Zhong, P. Liu, H. Hong, S. Wang, L. Xie, M. Lin, Y. Jiaerken, X. Luo, K. Li, Q. Zeng, L. Cui, J. Li, Y. Chen, and R. Zhang. Development and validation of a perivascular space segmentation method in multi-center datasets. *NeuroImage*, 298, 2024. doi: 10.1016/j.neuroimage.2024.120803. URL `https://www.scopus.com/inward/record.uri?eid=2-s2.0-85202211732&doi=10.1016%2fj.neuroimage.2024.120803&partnerID=40&md5=2e13c57014f4312234b6b8b9bf23dcf7`. cited By 0.

J. J. Iliff, M. J. Chen, B. A. Plog, D. M. Zeppenfeld, M. Soltero, L. Yang, I. Singh, R. Deane, and M. Nedergaard. Impairment of glymphatic pathway function promotes tau pathology after traumatic brain injury. *J. Neurosci.*, 34(49):16180–16193, Dec. 2014.

S. Ioffe and C. Szegedy. Batch normalization: Accelerating deep network training by reducing internal covariate shift. In F. Bach and D. Blei, editors, *Proceedings of the 32nd International Conference on Machine Learning*, volume 37 of *Proceedings of Machine Learning Research*, pages 448–456, Lille, France, 07–09 Jul 2015. PMLR. URL `https://proceedings.mlr.press/v37/ioffe15.html`.

M. Jenkinson, C. F. Beckmann, T. E. Behrens, M. W. Woolrich, and S. M. Smith. Fsl. *Neuroimage*, 62(2): 782–790, 2012.

T. Jerman, F. Pernuš, B. Likar, and Ž. Špiclin. Beyond frangi: an improved multiscale vesselness filter. In *Medical imaging 2015: Image processing*, volume 9413, pages 623–633. SPIE, 2015.

N. A. Jessen, A. S. F. Munk, I. Lundgaard, and M. Nedergaard. The glymphatic system: A beginner's guide. *Neurochem. Res.*, 40(12):2583–2599, Dec. 2015.

J. Jiang, V. Santhakumar, and X. Zhu. Editorial: Neuroinflammation in acquired epilepsy. *Front. Cell Dev. Biol.*, 10:1074537, Nov. 2022.

K. Karkoska, J. Gollamudi, R. Sawyer, D. Woo, and H. Hyacinth. Quantifying dilated perivascular spaces in children with sickle cell disease. *Pediatric Blood and Cancer*, 71(9), 2024. doi: 10.1002/pbc.31150. URL `https://www.scopus.com/inward/record.uri?eid=2-s2.0-85197583833&doi=10.1002%2fpbc.31150&partnerID=40&md5=f5ab7755f12e6e6e9587c453990bd57c`. cited By 0.

C. Kobylecki. Update on the diagnosis and management of parkinson's disease. *Clin. Med.*, 20(4):393–398, July 2020.

B. T. Kress, J. J. Iliff, M. Xia, M. Wang, H. S. Wei, D. Zeppenfeld, L. Xie, H. Kang, Q. Xu, J. A. Liew, B. A. Plog, F. Ding, R. Deane, and M. Nedergaard. Impairment of paravascular clearance pathways in the aging brain. *Ann. Neurol.*, 76(6):845–861, Dec. 2014.

R. M. Kwee and T. C. Kwee. Virchow-Robin spaces at MR imaging. *Radiographics*, 27(4):1071–1086, July 2007.

H. Lan, K. M. Lynch, R. Custer, N.-C. Shih, P. Sherlock, A. W. Toga, F. Sepehrband, and J. Choupan. Weakly supervised perivascular spaces segmentation with salient guidance of frangi filter. *Magnetic resonance in medicine*, 89(6):2419–2431, 2023.

A. Laveskog, R. Wang, L. Bronge, L. O. Wahlund, and C. Qiu. Perivascular spaces in old age: Assessment, distribution, and correlation with white matter hyperintensities. *American Journal of Neuroradiology*, 39: 70–76, 2018. doi: 10.3174/ajnr.A5455.

T.-Y. Lin, P. Goyal, R. Girshick, K. He, and P. Dollár. Focal loss for dense object detection. In *Proceedings of the IEEE international conference on computer vision*, pages 2980–2988, 2017.

Z. Luo, Y. Zhu, Y. Zhu, B. Liu, Y. Li, L. Yin, J. Liu, Z. Xu, H. Ren, and X. Yang. Cognitive function in parkinson's disease: associations with perivascular space in basal ganglia. *Neurol. Sci.*, Aug. 2024.

X. Ma, S. Li, C. Li, R. Wang, M. Chen, H. Chen, and W. Su. Diffusion tensor imaging along the perivascular space index in different stages of parkinson's disease. *Front. Aging Neurosci.*, 13:773951, Nov. 2021.

J.-C. Meng, M.-Q. Shen, Y.-L. Lu, H.-X. Feng, X.-Y. Chen, D.-Q. Xu, G.-H. Wu, Q.-Z. Cheng, L.-H. Wang, and Q. Gui. Correlation of glymphatic system abnormalities with parkinson's disease progression: a clinical study based on non-invasive fMRI. *J. Neurol.*, 271(1):457–471, Jan. 2024.

J. Moses, B. Sinclair, M. Law, T. O'Brien, and L. Vivash. Automated methods for detecting and quantitation of enlarged perivascular spaces on mri. *Journal of Magnetic Resonance Imaging*, 57(1):11–24, 2023. doi: 10.1002/jmri.28369. URL `https://www.scopus.com/inward/record.uri?eid=2-s2.0-85134498004&doi=10.1002%2fjmri.28369&partnerID=40&md5=9742f7ea535eb5f4d68ab1c167ae1a77`. cited By 13.

M. Nilashi, R. A. Abumalloh, S. Y. M. Yusuf, H. H. Thi, M. Alsulami, H. Abosaq, S. Alyami, and A. Alghamdi. Early diagnosis of parkinson's disease: A combined method using deep learning and neuro-fuzzy techniques. *Computational Biology and Chemistry*, 102:107788, 2023. ISSN 1476-9271. doi: https://doi.org/10.1016/j.compbiolchem.2022.107788. URL `https://www.sciencedirect.com/science/article/pii/S1476927122001682`.

M. B. Paradise, M. S. Beaudoin, L. Dawes, J. D. Crawford, W. Wen, H. Brodaty, and et al. Development and validation of a rating scale for perivascular spaces on 3t mri. *Journal of Neurological Sciences*, 409:116621, 2020. doi: 10.1016/j.jns.2019.116621.

S. H. Park, X. Zong, Y. Gao, W. Lin, and D. Shen. Segmentation of perivascular spaces in 7 t mr image using auto-context model with orientation-normalized features. *Neuroimage*, 134:223–235, 2016.

T. F. Patankar, D. Mitra, A. Varma, J. Snowden, D. Neary, and A. Jackson. Dilatation of the virchow-robin space is a sensitive indicator of cerebral microvascular disease: Study in elderly patients with dementia. *AJNR American Journal of Neuroradiology*, 26(6):1512–1520, 2005.

W. Pham, M. Lynch, G. Spitz, T. O'Brien, L. Vivash, B. Sinclair, and M. Law. A critical guide to the automated quantification of perivascular spaces in magnetic resonance imaging. *Frontiers in Neuroscience*, 16, 2022. doi: 10.3389/fnins.2022.1021311. URL `https://www.scopus.com/inward/record.uri?eid=2-s2.0-85145054407&doi=10.3389%2ffnins.2022.1021311&partnerID=40&md5=c5347d3b5e57f08d3be87209e7eedaae`. cited By 15.

G. Potter, Z. Morris, and J. Wardlaw. Guide prepared by enlarged perivascular spaces (epvs): A visual rating scale and user guide. Available online at: `https://www.ed.ac.uk/files/imports/fileManager/epvs-rating-scale-user-guide.pdf`, 2015. Accessed on Aug 17, 2022.

J. Ramirez, E. Gibson, A. Quddus, N. J. Lobaugh, A. Feinstein, B. Levine, C. J. M. Scott, N. Levy-Cooperman, F. Q. Gao, and S. E. Black. Lesion explorer: a comprehensive segmentation and parcellation package to obtain regional volumetrics for subcortical hyperintensities and intracranial tissue. *Neuroimage*, 54(2): 963–973, Jan. 2011.

T. Rashid, H. Liu, J. Ware, K. Li, J. Romero, E. Fadaee, I. Nasrallah, S. Hilal, R. Bryan, T. Hughes, C. Davatzikos, L. Launer, S. Seshadri, S. Heckbert, and M. Habes. Deep learning based detection of enlarged perivascular spaces on brain mri. *Neuroimage: Reports*, 3(1), 2023. doi: 10.1016/j.ynirp.2023.100162. URL `https://www.scopus.com/inward/record.uri?eid=2-s2.0-85151955962&doi=10.1016%2fj.ynirp.2023.100162&partnerID=40&md5=0590e36321b9971fa56dd78f55a597da`. cited By 11.

L. A. Ray, M. Pike, M. Simon, J. J. Iliff, and J. J. Heys. Quantitative analysis of macroscopic solute transport in the murine brain. *Fluids Barriers CNS*, 18(1):55, Dec. 2021.

O. Ronneberger, P. Fischer, and T. Brox. U-net: Convolutional networks for biomedical image segmentation. In N. Navab, J. Hornegger, W. M. Wells, and A. F. Frangi, editors, *Medical Image Computing and Computer-Assisted Intervention – MICCAI 2015*, pages 234–241, Cham, 2015. Springer International Publishing. ISBN 978-3-319-24574-4.

F. Sepehrband, G. Barisano, N. Sheikh-Bahaei, R. P. Cabeen, J. Choupan, M. Law, and A. W. Toga. Image processing approaches to enhance perivascular space visibility and quantification using mri. *Scientific reports*, 9(1):12351, 2019.

F. Sepehrband, G. Barisano, N. Sheikh-Bahaei, J. Choupan, R. P. Cabeen, K. M. Lynch, M. S. Crawford, H. Lan, W. J. Mack, H. C. Chui, et al. Volumetric distribution of perivascular space in relation to mild cognitive impairment. *Neurobiology of aging*, 99:28–43, 2021.

A. Shah, M. S. Al-Shaibani, M. Ahmad, and R. Bunyan. A bibliography of multiple sclerosis lesions detection methods using brain mris. *arXiv preprint arXiv:2302.09516*, 2023.

T. Shen, Y. Yue, S. Zhao, J. Xie, Y. Chen, J. Tian, W. Lv, C.-Y. Z. Lo, Y.-C. Hsu, T. Kober, et al. The role of brain perivascular space burden in early-stage parkinson's disease. *NPJ Parkinson's disease*, 7(1):12, 2021.

J. Spijkerman, J. Zwanenburg, W. Bouvy, M. Geerlings, G. Biessels, J. Hendrikse, P. Luijten, and H. Kuijf. Automatic quantification of perivascular spaces in t2-weighted images at 7 t mri. *Cerebral Circulation - Cognition and Behavior*, 3, 2022. doi: 10.1016/j.cccb.2022.

100142. URL https://www.scopus.com/inward/record.uri?eid=2-s2.0-85127977082&doi=10.1016%2fj.cccb.2022.100142&partnerID=40&md5=d8e7007bae9e32754817dc778190b3a3. cited By 9.

B. Vachha and S. Y. Huang. MRI with ultrahigh field strength and high-performance gradients: challenges and opportunities for clinical neuroimaging at 7 T and beyond. *Eur. Radiol. Exp.*, 5(1):35, Aug. 2021.

Y. Wan, W. Hu, J. Gan, L. Song, N. Wu, Y. Chen, and Z. Liu. Exploring the association between cerebral small-vessel diseases and motor symptoms in parkinson's disease. *Brain Behav.*, 9(4):e01219, Apr. 2019.

J. M. Wardlaw, E. E. Smith, G. J. Biessels, C. Cordonnier, F. Fazekas, R. Frayne, R. I. Lindley, J. T. O'Brien, F. Barkhof, O. R. Benavente, S. E. Black, C. Brayne, M. Breteler, H. Chabriat, C. Decarli, F.-E. de Leeuw, F. Doubal, M. Duering, N. C. Fox, S. Greenberg, V. Hachinski, I. Kilimann, V. Mok, R. van Oostenbrugge, L. Pantoni, O. Speck, B. C. M. Stephan, S. Teipel, A. Viswanathan, D. Werring, C. Chen, C. Smith, M. van Buchem, B. Norrving, P. B. Gorelick, M. Dichgans, and STandards for ReportIng Vascular changes on nEuroimaging (STRIVE v1). Neuroimaging standards for research into small vessel disease and its contribution to ageing and neurodegeneration. *Lancet Neurol.*, 12(8):822–838, Aug. 2013.

J. M. Wardlaw, H. Benveniste, M. Nedergaard, B. V. Zlokovic, H. Mestre, H. Lee, F. N. Doubal, R. Brown, J. Ramirez, B. J. MacIntosh, A. Tannenbaum, L. Ballerini, R. L. Rungta, D. Boido, M. Sweeney, A. Montagne, S. Charpak, A. Joutel, K. J. Smith, S. E. Black, and colleagues from the Fondation Leducq Transatlantic Network of Excellence on the Role of the Perivascular Space in Cerebral Small Vessel Disease. Perivascular spaces in the brain: anatomy, physiology and pathology. *Nat. Rev. Neurol.*, 16(3):137–153, Mar. 2020.

J. Yao, T. Huang, Y. Tian, H. Zhao, R. Li, X. Yin, S. Shang, and Y.-C. Chen. Early detection of dopaminergic dysfunction and glymphatic system impairment in parkinson's disease. *Parkinsonism Relat. Disord.*, 127 (107089):107089, Oct. 2024.

Appendix A

List of acronyms

Below is a list of acronyms used throughout this thesis:

Acronym	**Definition**
ADNI	Alzheimer's Disease Neuroimaging Initiative
AI	Artificial Intelligence
AvgPool3D	3D Average Pooling Layer
BN	Batch Normalization
BET	Brain Extraction Tool
CCA	Connected Component Analysis
CNN	Convolutional Neural Network
Concat	Concatenation Layer
CSF	Cerebrospinal Fluid
CSO	Centrum Semiovale
CSVD	Cerebral Small-Vessel Disease
DAG	Directed Acyclic Graph
DL	Deep Learning
dMRI	Diffusion Magnetic Modalities Imaging
dPVS	Dilated Perivascular Spaces
DSC	Dice Similarity Coefficient
DTI	Diffusion Tensor Imaging
DTI-ALPS	Diffusion Tensor Image Analysis Along Perivascular Space
DWM	Deep White Matter
FL	Focal Loss
FLAIR	Fluid-Attenuated Inversion Recovery
FLIRT	FMRIB's Linear Image Registration Tool
fMRI	Functional Magnetic Resonance Imaging
FOG	Freezing of Gait
FSL	FMRIB Software Library
GM	Gray Matter
HD	Huntington's Disease
ICC	Intraclass Correlation Coefficients
ISF	Interstitial Fluid
kNN	k-Nearest Neighbors
LEDD	Levodopa Equivalent Daily Dose
MESA	Multi-Ethnic Study of Atherosclerosis
ML	Machine Learning
MPRAGE	Magnetization Prepared Rapid Acquisition Gradient Echo
MRI	Magnetic Resonance Imaging
ePVS	Enlarged Perivascular Spaces
PD	Parkinson's Disease
PPV	Positive Predictive Value

PPTS	Post-Traumatic Syringomyelia
PVE	Partial Volume Estimation Maps
PVS	Perivascular Spaces
ROI	Region of Interest
RX	Radiography
SCD	Sickle Cell Disease
SIT	Silent Cerebral Infarct Transfusion
SpatialDrop3D	3D Spatial Dropout Layer
STRIVE	Standards for Reporting Vascular Changes on Neuroimaging
SVD	Small Vessel Disease
TransposeConv3D	3D Transposed Convolution Layer
TSE	Turbo Spin Echo
UDPRS	Unified Parkinson's Disease Rating Scale
WM	White Matter
WMH	White Matter Hyperintensities
WDL	Weighted Dice Loss

This appendix serves as a reference for readers unfamiliar with the abbreviations used in this thesis.

Appendix B

Ethical approval

The study was designed as a prospective case-control investigation and received approval from the Ethical Committee of Fondazione Policlinico Universitario Campus Bio-Medico (N. SC 2022.086).

Written informed consent was obtained from all participants prior to their involvement, ensuring their understanding and voluntary participation. This study is a feasibility study and its results will not affect the clinical course of the patients.